

Chapter 3. Wavelet analysis as a single-spacecraft method

Single-spacecraft measurements have been used in the identification of small-scale magnetic structures (Pecora et al., 2019; Telloni et al., 2012; Hu et al., 2018; Zheng and Hu, 2018; Zhao et al., 2020). The time series data can be treated as a spatial snapshot due to the effective stationary state of the plasma medium traversed by a spacecraft relative to the fast-moving solar wind. Time series data are transformed directly to spatial distributions (Taylor, 1938). Therefore, time-frequency transforms, such as wavelet transforms, are conceivably useful for analyzing features of in situ spacecraft time series at different frequencies over time (Torrence and Compo, 1998). Specifically the power spectra associated with a number of selected MHD quantities are derived to characterize the underlying magnetic structures.

3.1 Wavelet transforms

Wavelet transforms are used to analyze time series with non-stationary power at different frequencies (Torrence and Compo, 1998) using non-orthogonal wavelet basis functions. Assuming a continuous signal as a function of time t ,

$x = x(t)$, the continuous wavelet transform is defined as

$$W(s, \tau) = \frac{1}{|s|^{1/2}} \int_{-\infty}^{\infty} x(t) \psi^* \left(\frac{t - \tau}{s} \right) dt. \quad (3.1)$$

Here ψ^* is the complex conjugate of the wavelet basis function $\psi(t)$, which is a function that must be localized in time and frequency space, and has zero mean (Torrence and Compo, 1998).

As usual, with a discrete set of data points $x_n = x(t_n)$ with time resolution δt , the continuous wavelet transform takes the discrete form

$$W_n(s, t) = \sum_{n'=0}^{N-1} x_{n'} \psi^* \left[\frac{(n' - n) \delta t}{s} \right]. \quad (3.2)$$

In practice, discrete wavelet transforms are implemented for time series data by dilating the scale s and translating along the time index n . This results in a two dimensional array of the wavelet transform. The scales are chosen such that

$$J = \frac{\log_2 \left(\frac{N \delta t}{s_0} \right)}{d_j} \quad (3.3)$$

$$s_j = s_0 2^{j d_j}, \quad j = 0, \dots, J \quad (3.4)$$

where $s_0 = 2\delta t$ and the choice of d_j is sufficiently small for the width of the wavelet basis function in spectral space. The Morlet wavelet given in Equation (3.5) is a good wavelet base because it is complex and has good frequency resolution, thus it is frequently used in small-scale flux rope identification (Telloni et al., 2012,

2013; Zhao et al., 2020; Farge, 1992):

$$\psi_0(\eta) = \pi^{-1/4} e^{i\omega_0\eta} e^{-\eta^2/2}. \quad (3.5)$$

Figure 3.1 visually demonstrates the typical transform of a time series data set from the time domain to a time-frequency domain, including the Fourier transform and the wavelet transform. Wavelet transforms take a one-dimensional time series (top left corner of Figure 3.1) and transform it into a two-dimensional series (bottom right corner of Figure 3.1), whereas the Fourier transform applied to a one-dimensional time series yields a one-dimensional series in the frequency domain (top right corner of Figure 3.1). The Fourier transform decomposes a time series function into a combination of the frequencies present in the data set (Farge, 1992). The Fourier transform of a time series $x(t)$ into its frequency domain (index k) is

$$F(k) = \int_{-\infty}^{\infty} x(t) e^{-2\pi i k t / N} dt, \quad (3.6)$$

and with discrete data $x_n = x(t_n)$, it takes the form

$$F_n(k) = \frac{1}{N} \sum_{n=0}^{N-1} x_n e^{-2\pi i k n / N}. \quad (3.7)$$

A short time Fourier transform (bottom left corner of Figure 3.1) can produce a two-dimensional time-frequency domain, but by segmenting the time series and performing a Fourier transform over the segments, the method only yields identical time-frequency domains, for each respective time segment. Fourier transforms

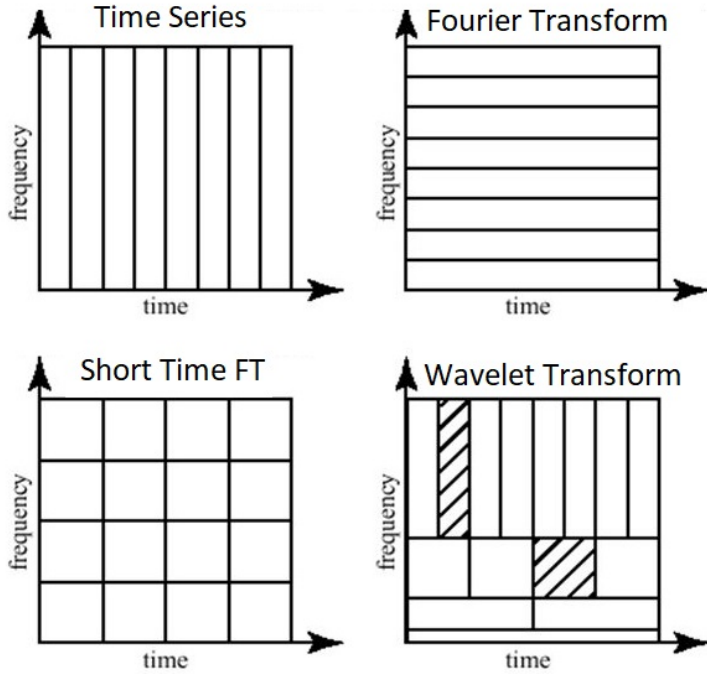


Figure 3.1: Time and frequency resolutions of different transforms applied to a one-dimensional time series dataset. The wavelet transform (bottom right) has non-uniform frequency and time resolution.

theoretically retain all the ‘information’ about an equation, but discrete Fourier transforms are a summation over a finite set and therefore are not as accurate.

3.2 MHD quantities

The magnetic field lines in flux ropes are twisted such that they preside in a tube-like configuration. Thus, flux ropes carry magnetohydrodynamic (MHD) quantities such as cross helicity H_c and magnetic helicity H_m , as well as residual

energy E_r , defined as

$$H_c = \frac{1}{2} \int \mathbf{v} \cdot \mathbf{b} \, d^3\mathbf{r} \quad (3.8)$$

$$H_m = \int \mathbf{A} \cdot \mathbf{B} \, d^3\mathbf{r} \quad (3.9)$$

$$E_r = \frac{1}{2} [\langle \mathbf{v}^2 \rangle - \langle \mathbf{b}^2 \rangle], \quad (3.10)$$

where $\mathbf{B}(\mathbf{x}, t)$ is the magnetic field, $\mathbf{A}(\mathbf{x}, t)$ is the magnetic vector potential, and $\mathbf{v}(\mathbf{x}, t)$ and $\mathbf{b}(\mathbf{x}, t)$ are the fluctuating velocity and magnetic field in Alfvén units. Cross helicity describes the measure of alignment between magnetic and velocity fluctuations, while magnetic helicity describes the “knottedness” of the magnetic field lines (Matthaeus and Goldstein, 1982). High magnetic helicity is a signature of flux ropes, and often accompanied by low cross helicity (Zhao et al., 2020). Residual energy describes the imbalance between magnetic and kinetic energy, and thus according to (3.10), a negative residual energy will characterize an event with higher magnetic energy.

Normalized MHD quantities give insight into the nature of magnetic field structures, and allow us to identify and characterize these events. Approximated in the time domain, the normalized cross helicity and residual energy can be calculated using

$$\sigma_c = \frac{2\langle \mathbf{v} \cdot \mathbf{b} \rangle}{\langle \mathbf{v}^2 \rangle + \langle \mathbf{b}^2 \rangle} \quad (3.11)$$

$$\sigma_r = \frac{\langle \mathbf{v}^2 \rangle - \langle \mathbf{b}^2 \rangle}{\langle \mathbf{v}^2 \rangle + \langle \mathbf{b}^2 \rangle} \quad (3.12)$$

where \mathbf{v} is the remaining flow in the de Hoffman-Teller frame. Single spacecraft measurements cannot be used directly calculate reduced magnetic helicity, therefore other methods are required to approximate this quantity. The power spectral density of a time series describes the distribution of the energy across the frequency components of a signal. Matthaeus and Goldstein (1982) showed that a form of the magnetic helicity can be calculated using single spacecraft measurements by utilizing the power spectral density. This can often be done in a similar fashion using wavelet transforms (Telloni et al., 2012, 2013). The continuous wavelet transform of a one-dimensional time series yields the two-dimensional time-scale spectrogram for a finite time period. This shows how the amplitude of a feature versus the scale varies with time, therefore making it useful in studying the features associated with multi-scale structures. The so-called reduced form of the magnetic helicity gives quantitative information about the magnetic helicity density along the radial dimension, X , and is calculated with Fourier transforms of the Y - and Z -components of the magnetic field, $\tilde{F}(B_Y)$ and $\tilde{F}(B_Z)$,

$$H_m(k) = \frac{2\text{Im}[S_{YZ}(k)]}{k} = \frac{2\text{Im}\left[\tilde{F}^*(B_Y)\tilde{F}(B_Z)\right]}{k}, \quad (3.13)$$

where $S_{YZ}(k)$ is one element of the reduced magnetic power spectral density tensor (Matthaeus and Goldstein, 1982). Telloni et al. (2012) showed that taking X along the radial direction from the sun, wavelet transforms of the magnetic field Y - and Z -components, the Elsässer variables Z^\pm , and kinetic and magnetic energies enable an efficient way to calculate the reduced normalized magnetic

helicity σ_m , cross helicity σ_c , and residual energy σ_r , corresponding to equations (3.8)-(3.10):

$$\sigma_m(k, t) = 2 \frac{\text{Im} [W_Y(k, t) W_Z^*(k, t)]}{|W_X(k, t)|^2 + |W_Y(k, t)|^2 + |W_Z(k, t)|^2}, \quad (3.14)$$

$$\sigma_c(k, t) = \frac{W^+(k, t) - W^-(k, t)}{W^+(k, t) + W^-(k, t)}, \quad (3.15)$$

$$\sigma_r(k, t) = \frac{W_{kin}(k, t) - W_{mag}(k, t)}{W_{kin}(k, t) + W_{mag}(k, t)}. \quad (3.16)$$

Here $W_X(k, t), W_Y(k, t), W_Z(k, t), W^+(k, t)$, and $W^-(k, t)$ are the wavelet transforms of B_X, B_Y, B_Z, Z^+ , and Z^- , respectively. The Elsässer variables, $Z^\pm = \mathbf{v} \pm \mathbf{b}$, are the combination of the velocity and magnetic field fluctuations in Alfvén units. $W_{kin}(k, t)$ and $W_{mag}(k, t)$ are the sums of the power of the wavelet transforms of the components of the velocity and magnetic field (in Alfvén units). Equations (3.14)-(3.16) can also be written in terms of scale and time :

$$\sigma_m(s, t) = 2 \frac{V_{X0} \text{Im} [W_Y(s, t) W_Z^*(s, t)]}{V_0 (|W_X(s, t)|^2 + |W_Y(s, t)|^2 + |W_Z(s, t)|^2)}, \quad (3.17)$$

$$\sigma_c(s, t) = \frac{W^+(s, t) - W^-(s, t)}{W^+(s, t) + W^-(s, t)}, \quad (3.18)$$

$$\sigma_r(s, t) = \frac{W_{kin}(s, t) - W_{mag}(s, t)}{W_{kin}(s, t) + W_{mag}(s, t)}. \quad (3.19)$$

since $\mathbf{k} \parallel \mathbf{V}_0$ (Zhao, L.-L. et al., 2021; Horbury et al., 2008; Taylor, 1938), where \mathbf{V}_0 is the average plasma velocity. Equation 3.17 only shows the first term of the

trace of the power spectrum because the radial component is dominant over the tangential component at 1 AU.

3.3 Algorithm for identification of magnetic structures

In Figure 3.2, the time series of the magnetic field and plasma parameters from 10:20-13:30 UT on 9 November 2019 are shown. Panels (a) and (b) show the magnetic field and velocity components of the time period, with magnetic field magnitude reaching a maximum of about 20 nT and a flow velocity deflected from the Sun-Earth direction. Panel (c) shows relatively high proton density, varying from 20 to 30 cm^{-3} , and proton temperature of $1\text{-}2\times 10^6 \text{ K}$, which is typical for magnetosheath plasma. Panel (d) shows the Alfvén speed and the bulk plasma speed with a mean value for this 3 hour period (193 km/s) subtracted. Panel (e) shows the proton beta, which is between approximately 1-100. Panel (f) of Figure 3.2 displays the spectrogram reduced magnetic helicity, which describes the “knottedness” of the magnetic field lines. Panel (g) shows the normalized measure of alignment between magnetic and velocity fluctuations, reduced cross helicity, and panel (h) shows the imbalance between magnetic and kinetic energy, or reduced residual energy (Matthaeus and Goldstein, 1982). These spectrograms show how the reduced MHD quantities vary in time and frequency, thus allowing us to search them for characteristics that are distinctive to different types of magnetic structures.

Structures with local enhanced magnetic helicity are identified with specific criteria: (i) magnetic helicity with absolute values greater than 0.75, (ii)

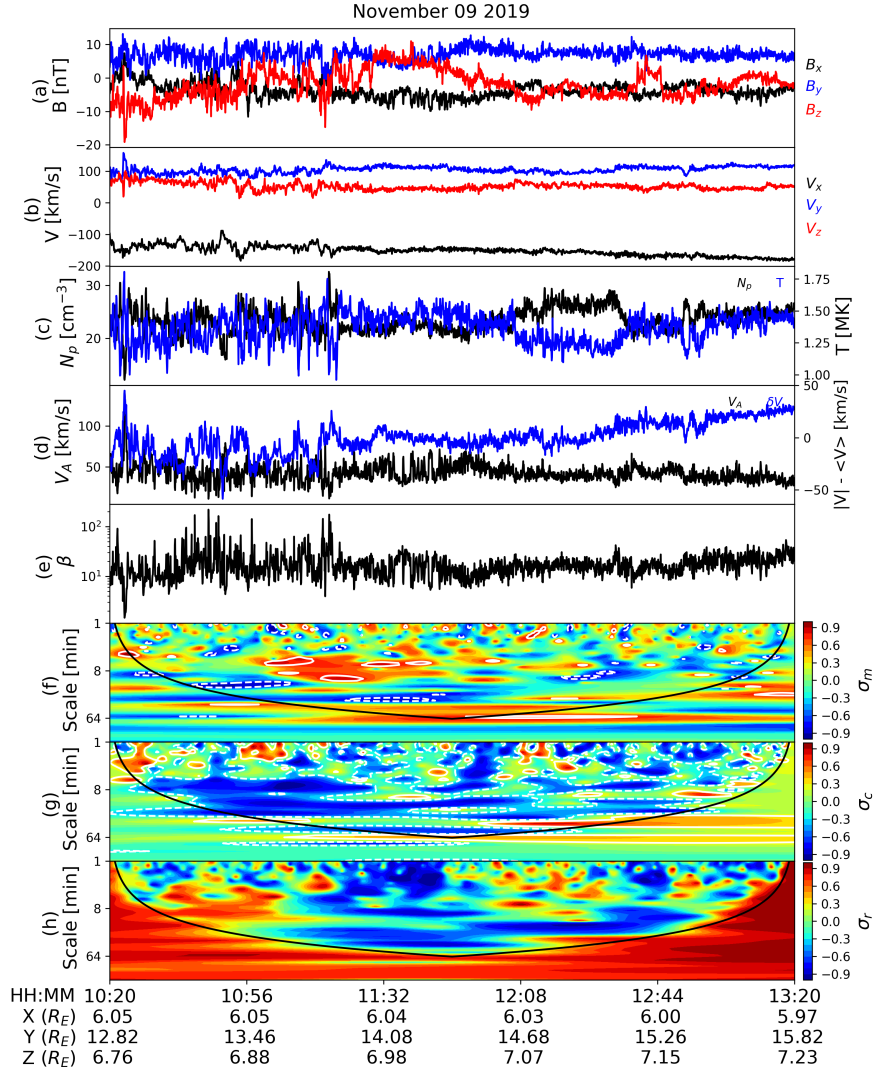


Figure 3.2: Time series of (a) magnetic field, (b) velocity, (c) plasma density and temperature, (d) Alfvén speed and velocity fluctuations, (e) plasma beta, and spectrograms of the normalized (f) reduced magnetic helicity, (g) cross helicity, and (h) residual energy found by wavelet analysis, across multiples scales (as indicated by the vertical axes), during a 3 hour period that MMS-1 was in the magnetosheath on 9 November 2019. White contours in panel (f) and (g) represent regions of high reduced magnetic helicity ($|\sigma_m| \geq 0.75$) and regions of low reduced cross helicity ($|\sigma_c| \leq 0.3$), respectively. The black curved line in panels (f)-(h) is the cone of influence.

duration between 30 seconds and 3 hours, and (iii) if the event was within the cone of influence, which arises because of finite data segment length (Torrence and Compo, 1998). I calculate reduced, normalized forms of magnetic helicity σ_m , cross helicity σ_c , and residual energy σ_r in 2400-point windows (~ 3 hours for MMS and ~ 2 hours for THEMIS) across the hours-long periods identified in the solar wind and magnetosheath. Figure 3.3 displays the spectrograms of reduced magnetic helicity from 10:20-13:30 UT and 11:05-14:05 UT on 9 November 2019. These intervals are calculated from the time series in Figure 3.2. Events identified with the wavelet analysis method are marked with a grey interval. The black contours represent event candidates with $|\sigma_m| \geq 0.75$ whereas the white contours indicate events that were established in the final event list. Inside the white contours, a white “X” marks the absolute local maximum, and the yellow annotations and dashed lines indicate the scale corresponding to a maximum. This scale is taken as the duration of the event, and the time of the peak in reduced σ_c is taken to the time-wise midpoint of the event. Therefore, the event interval start time will be the time of the peak in $|\sigma_m|$ minus half of the scale size of the peak. The events identified from this wavelet analysis can be further characterized by implementing the criteria that the events have (iv) corresponding cross helicity with absolute value less than 0.3, to ensure that there is low level of velocity fluctuations and/or (v) negative residual energy, which indicates that the magnetic energy is dominant.

It can be seen that not all grey event intervals have a white contour and marker for the maximum σ_c . This is because of the windowed analysis: as the

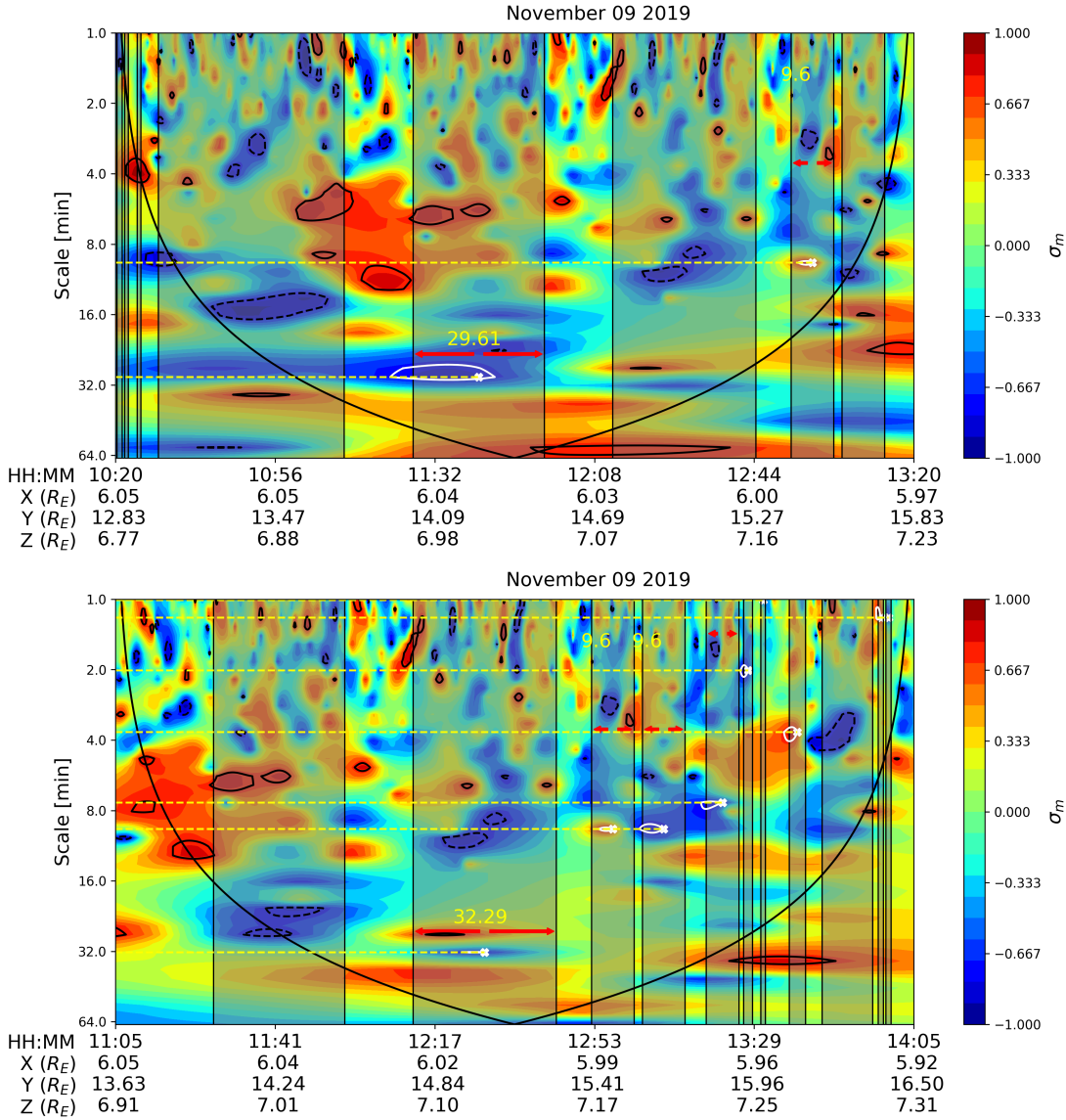


Figure 3.3: Spectrograms of reduced magnetic helicity over two overlapping 3-hour period from MMS-1 data on 9 November 2019. Demarcated intervals are identified events via wavelet analysis. Black contours represent regions of high reduced magnetic helicity ($|\sigma_m| \geq 0.75$). White contours represent regions of $|\sigma_m| \geq 0.75$ where the maximum inside the contour is an established event. Yellow dashed lines connect the maximum of the contour to the x-axis (scale) of the maximum. Red arrows indicate half of the scale (duration) on either side of the peak of σ_c . The black curved line is the cone of influence.

maxima in reduced magnetic helicity are recorded in each window, there will be overlapping events identified. The intervals in Figure 3.3 are overlapping by 600 data points (45 minutes for MMS data). After all the windows are searched, the compiled event list is then processed to eliminate overlapping events. By comparing two adjacently overlapping events and keeping the one with the highest maximum $|\sigma_m|$, this is repeated until there are no overlapping events left. Figure 3.4 shows an example of event intervals identified via the wavelet algorithm (with the criteria $|\sigma_m| \geq 0.75$) overlaid the corresponding time series and spectrogram of the reduced magnetic helicity in the magnetosheath during 9 November 2019. There are 11 events identified by the wavelet algorithm during this 3 hour period. The duration of these events range from 1 minute to 32.29 minutes, with an average duration of 9.913 minutes. The average maximum magnetic field of the events is 12.23 nT. The average absolute maximum (normalized) magnetic helicity of these 11 events is 0.83. 6 events in this period have $|\sigma_c| \leq 0.3$, and one of those events has $\sigma_r < 0$. Of remaining 5 events, none have $\sigma_r < 0$.

3.4 Event categorization

There were 4260 events identified from the wavelet analysis in the magnetosheath across 1051 hours. For the solar wind, there were 3193 events identified across 676 hours via wavelet analysis. The occurrence rate for events in the solar wind from the wavelet method is about 4.7 events/hour and for the magnetosheath the corresponding rate is about 4.0 events/hour. Table 3.1 summarizes the events identified with the wavelet analysis algorithm.

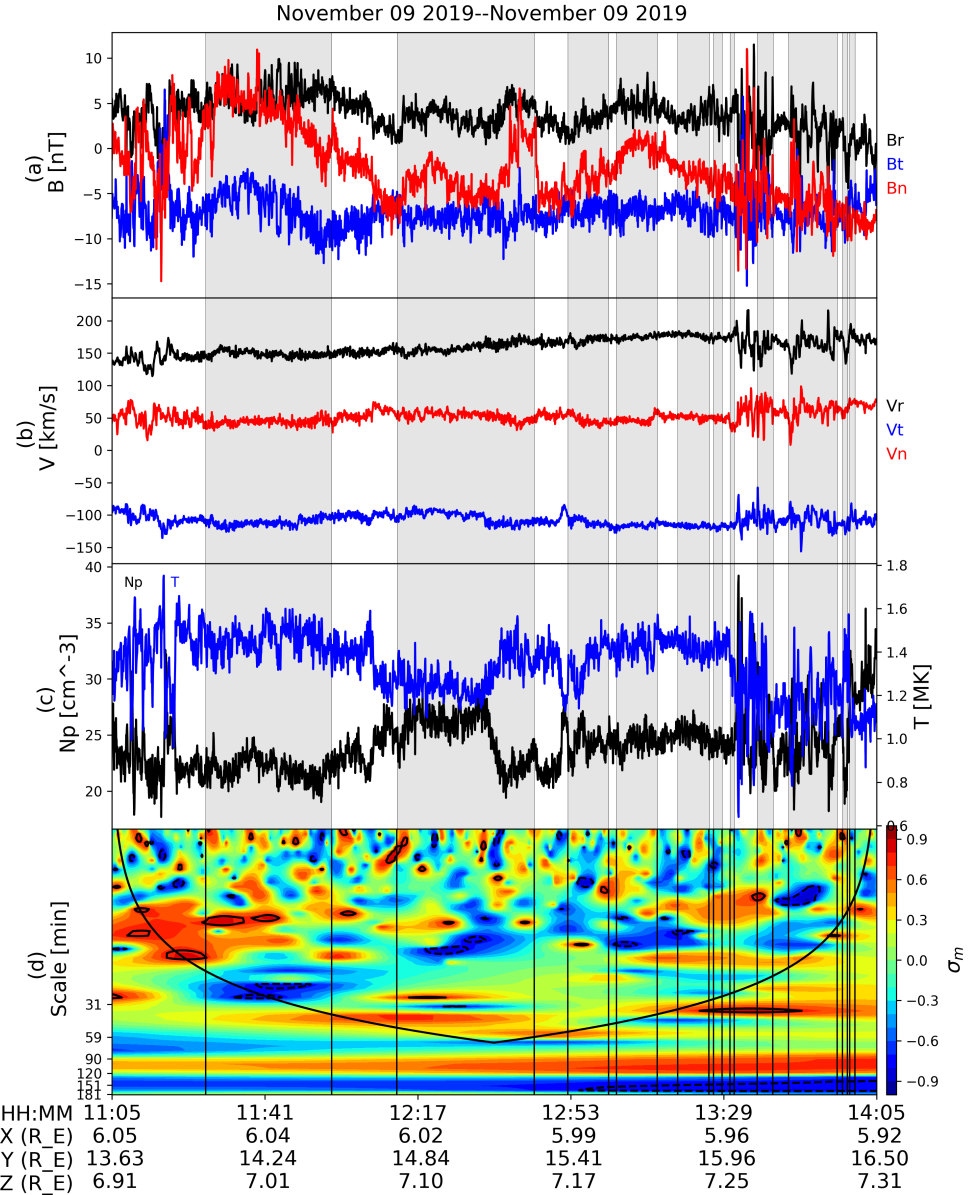


Figure 3.4: Portion of the 9 November 2019 time series and reduced magnetic helicity spectrogram. The grey intervals representing events identified with wavelet analysis meeting the criteria $|\sigma_m| \geq 0.75$.

Table 3.1: Summary table for identified events in the solar wind and magnetosheath via wavelet analysis as described in Section 3.3.

	Observation period [hrs]	Events	Event rate [#/hour]
<i>Solar wind</i>	676	3193	4.723
<i>Magnetosheath</i>	1051	4260	4.053

Properties of the magnetic structures are recorded during the identification process. Table 3.2 summarizes the statistical values for the identified events. The average duration of the events is 7.40 and 8.76 minutes for the solar wind and magnetosheath, respectively. In the solar wind, there are a large number of events with an average magnetic field of less than 10 nT, whereas in the magnetosheath there are relatively much fewer events with $\langle B \rangle < 10$ nT. The median magnetic field magnitude in the solar wind is 4.6 nT for events identified with wavelet analysis, and in the magnetosheath this number is 16.5 nT. As shown in Table 3.2, the duration of the events has similar ranges for the two regions. However, for the scale sizes of the events in the magnetosheath, they range from ~ 1507 km to 1.287×10^6 km, with a median and mean of 3.441×10^4 km, $\sim 5.4 R_E$ and 1.108×10^5 km, $\sim 17.4 R_E$, respectively. In the solar wind, the corresponding values are from 8975.2 km to 2.107×10^6 km, and a median (mean) of 5.444×10^5 (1.612×10^5) km, ~ 8.5 (25.3) R_E . It is important to note that the calculations of scale size cannot be considered as physically reliable as the calculations from the GS-based method since the specificity of the wavelet analysis identification

Table 3.2: Statistical values for the physical quantities of the structures identified in the magnetosheath (top) and solar wind (bottom) with wavelet analysis.

	Minimum	Maximum	Mean	Median	Std. Dev.
Duration [min]	0.517	59.221	8.761	2.617	12.6
Velocity [km/s]	13.653	567.539	220.381	214.361	75.4
Temperature [10^6 K]	0.601	31.611	2.908	2.200	2.3
$\langle B \rangle$ [nT]	2.344	85.790	20.213	16.473	12.2
Scale size [km]	1506.944	1.287×10^6	1.108×10^5	3.441×10^4	1.6×10^5
Duration [min]	0.560	59.221	7.402	2.400	10.6
Velocity [km/s]	235.264	664.001	367.580	342.591	87.4
Temperature [10^6 K]	0.114	16.946	2.600	0.685	3.4
$\langle B \rangle$ [nT]	0.543	29.372	4.935	4.576	2.5
Scale size [km]	8975.252	2.107×10^6	1.612×10^5	5.444×10^4	2.4×10^5

method relies on factors such as data segment length and choice of wavelet basis, in addition to the calculations being done in the spacecraft frame of reference.

Table 3.3 categorizes the events identified via wavelet analysis based on meeting certain MHD criteria. Over half of the events in the solar wind have characteristics of static flux ropes ($|\sigma_m| \geq 0.75$, $|\sigma_c| \leq 0.3$, $\sigma_r < 0$), whereas in the magnetosheath there are fewer events (approximately one-third) that meet these criteria. The distribution of the reduced cross helicity and residual energy

Table 3.3: Summary table of events meeting certain MHD criteria for events identified via wavelet analysis in the magnetosheath and solar wind.

	Solar wind	Magnetosheath
$ \sigma_m \geq 0.75$	3193	4260
$ \sigma_m \geq 0.75, \sigma_c \leq 0.3$	1821	2490
$ \sigma_m \geq 0.75, \sigma_r < 0$	2156	2468
$ \sigma_m \geq 0.75, \sigma_c \leq 0.3, \sigma_r < 0$	1144	1567

for all identified events in the solar wind and magnetosheath is shown in Figure 3.5. The histogram shows the averaged, reduced MHD quantities of the events identified by the wavelet method. Figure 3.5 shows flatter distributions of reduced cross helicity σ_c in the magnetosheath than in the solar wind. The reduced cross helicity distribution maintains a peak around $\sigma_c = 0$ in both regions in Figure 3.5, with the solar wind having a steeper shape. The reduced residual energy has a peak at $\sigma_r = -1$, with values that are nearly evenly distributed between $(-1, 1)$.

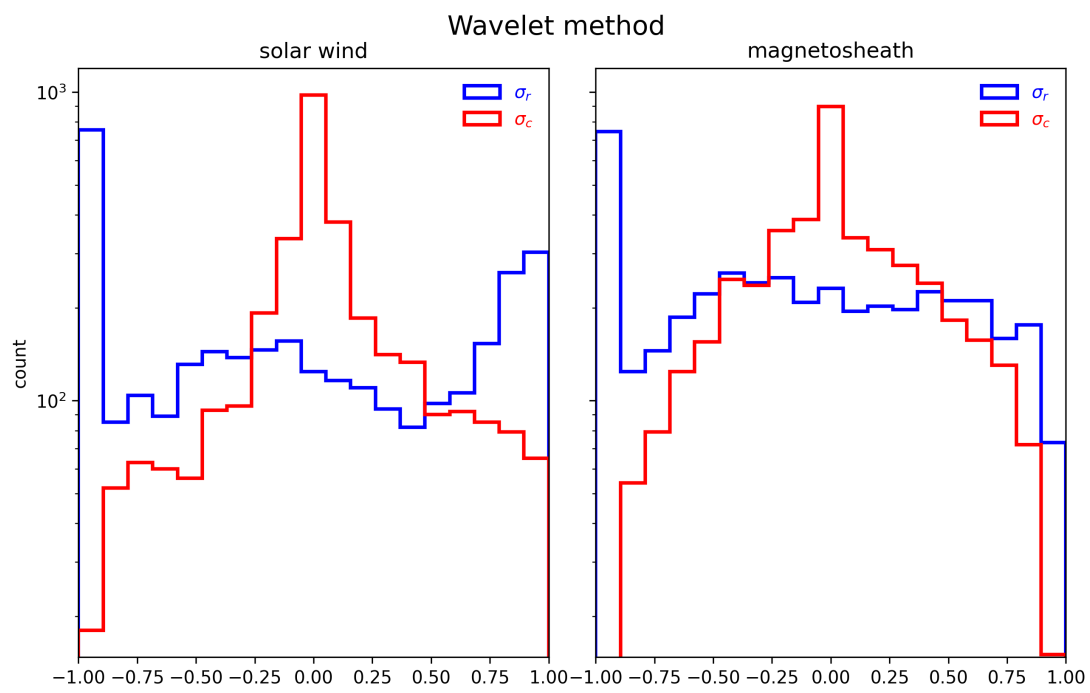


Figure 3.5: Histograms of reduced cross helicity σ_c (red) and reduced residual energy σ_r (blue) for all solar wind (left) and magnetosheath events (right) identified via the wavelet method.

Chapter 4. Grad-Shafranov reconstruction and automated identification algorithm

4.1 The Grad-Shafranov equation

The Grad-Shafranov (GS) equation describes the force balance between the Lorentz force and the gradient of the thermal pressure p (Sonnerup and Guo, 1996; Hau and Sonnerup, 1999) in two spatial dimensions (x, y) with $\frac{\partial}{\partial z} = 0$, as given below,

$$\nabla^2 A = \frac{\partial^2 A}{\partial x^2} + \frac{\partial^2 A}{\partial y^2} = -\mu_0 \frac{dP_t}{dA} = -\mu_0 \frac{d}{dA} \left(p + \frac{B_z^2}{2\mu_0} \right). \quad (4.1)$$

Here, $A_z(x, y) = A$ is the magnetic scalar potential, B_z is the z -component of the magnetic field, and P_t is the total pressure (thermal plus magnetic).

4.1.1 Derivation of the original GS equation

Starting with the magnetic field expressed by the magnetic vector potential and balancing the gradient of the pressure with the Lorentz force in 2D ($\frac{\partial}{\partial z} = 0$),

$$\mathbf{B} = \nabla \times \mathbf{A} = \nabla A_z \times \hat{z} + B_z \hat{z} \quad (4.2)$$

$$\nabla p = \mathbf{j} \times \mathbf{B} = j_z \hat{z} \times \mathbf{B}_\perp + \mathbf{j}_\perp \times B_z \hat{z} \quad (4.3)$$

Using Ampere's law to determine the components of the current density \mathbf{j} ,

$$\begin{aligned} \nabla \times \mathbf{B} &= \mu_0 \mathbf{j} \\ \nabla \times (\nabla \times \mathbf{A}) &= \mu_0 \mathbf{j} \\ \nabla \times [\nabla A_z \times \hat{z} + B_z \hat{z}] &= \mu_0 [j_z \hat{z} + \mathbf{j}_\perp] \end{aligned} \quad (4.4)$$

The \hat{z} and perpendicular components of the current density are then found by,

$$\begin{aligned} \mu_0 j_z \hat{z} &= \nabla \times (\nabla A_z \times \hat{z}) \\ &= (\nabla \cdot \hat{z}) \nabla A_z - (\nabla \cdot \nabla A_z) \hat{z} \\ j_z \hat{z} &= -\frac{1}{\mu_0} \nabla^2 A_z \hat{z} \end{aligned} \quad (4.5)$$

$$\begin{aligned} \mu_0 \mathbf{j}_\perp &= \nabla \times B_z \hat{z} \\ \mathbf{j}_\perp &= \frac{1}{\mu_0} \nabla B_z \times \hat{z} \end{aligned} \quad (4.6)$$

Simplifying the \hat{z} and perpendicular terms of the pressure gradient (4.3),

$$\begin{aligned} j_z \hat{z} \times \mathbf{B}_\perp &= -\frac{1}{\mu_0} \nabla^2 A_z \hat{z} \times (\nabla A_z \times \hat{z}) \\ &= -\frac{1}{\mu_0} [(\nabla^2 A_z \hat{z} \cdot \hat{z}) \nabla A_z - (\nabla^2 A_z \hat{z} \cdot \nabla A_z) \hat{z}] \\ &= -\frac{1}{\mu_0} (\nabla^2 A_z) \nabla A_z \end{aligned} \quad (4.7)$$

$$\begin{aligned}
\mathbf{j}_\perp \times B_z \hat{z} &= \left(\frac{1}{\mu_0} \nabla B_z \times \hat{z} \right) \times B_z \hat{z} \\
&= \frac{1}{\mu_0} [(B_z \hat{z} \cdot \nabla B_z) \hat{z} - (B_z \hat{z} \cdot \nabla B_z) \hat{z}] \\
&= -\frac{1}{\mu_0} B_z \nabla B_z
\end{aligned} \tag{4.8}$$

and substituting them into the respective right hand side of (4.3):

$$\begin{aligned}
\nabla p &= -\frac{1}{\mu_0} (\nabla^2 A_z) \nabla A_z - \frac{1}{\mu_0} B_z \nabla B_z \\
(\nabla^2 A_z) \nabla A_z &= -\mu_0 \left(\nabla p + \frac{1}{\mu_0} B_z \nabla B_z \right) \\
(\nabla^2 A_z) \nabla A_z &= -\mu_0 \left(\frac{dp}{dA} \nabla A_z + \frac{1}{\mu_0} B_z \frac{dB_z}{dA} \nabla A_z \right) \\
\nabla^2 A_z &= -\mu_0 \left(\frac{dp}{dA} + \frac{1}{\mu_0} \frac{dB_z}{dA} \right)
\end{aligned}$$

Replacing A with A_z for the sake of simplicity, we arrive at the form for the Grad-Shafranov equation (4.1),

$$\nabla^2 A = -\mu_0 \frac{d}{dA} \left(p + \frac{B_z^2}{2\mu_0} \right). \tag{4.9}$$

4.1.2 Derivation of the extended GS equation

The implementation by Chen et al. (2021) utilizes the extended GS method, which still seeks to find the double-folding pattern between two P'_t versus A' curves, but with $A' = (1 - \alpha)A$ and $P'_t = (1 - \alpha)p + (1 - \alpha)^2 \frac{B_z^2}{2\mu_0} + \alpha(1 - \alpha) \frac{B^2}{2\mu_0}$. The factor α is a proportionality constant, which for a field-aligned flow is the average Alfvén Mach number squared, $\alpha = \langle M_A \rangle^2 \approx \text{const}$ in a frame of reference

moving with the structure governed by the GS equation. The extended GS (or GS-type) equation (Teh, 2018; Sonnerup et al., 2006) is:

$$\nabla^2 A' = -\mu_0 \frac{d}{dA'} \left[(1-\alpha)p + (1-\alpha)^2 \frac{B_z^2}{2\mu_0} + \alpha(1-\alpha) \frac{B^2}{2\mu_0} \right] \quad (4.10)$$

which simplifies to the original GS equation (4.1) when $\alpha \equiv 0$. The extended GS method allows us to identify structures with significant remaining plasma flow aligned with the local magnetic field in a proper frame of reference (Chen and Hu, 2022).

For a structure with a field-aligned flow, the momentum equation becomes

$$\begin{aligned} -\nabla p \times \mathbf{j} \times \mathbf{B} &= \rho \left[\frac{\nabla v^2}{2} - \mathbf{v} \times (\nabla \times \mathbf{v}) \right] \\ \rho (\nabla \times \mathbf{v}) \times \mathbf{v} - \mathbf{j} \times \mathbf{B} &= -\nabla p - \rho \frac{\nabla v^2}{2}. \end{aligned} \quad (4.11)$$

Expanding the left hand side of (4.11), it becomes

$$\begin{aligned} &\rho (\nabla \times \mathbf{v}) \times \mathbf{v} - \frac{1}{\mu_0} (\nabla \times \mathbf{B}) \times \mathbf{B} \\ &\rho [-\nabla \mathbf{v} \cdot \mathbf{v} + (\mathbf{v} \cdot \nabla) \mathbf{v}] + \frac{1}{\mu_0} [\nabla \mathbf{B} \cdot \mathbf{B} - (\mathbf{B} \cdot \nabla) \mathbf{B}] \\ &\rho [-\nabla \mathbf{v} \cdot \mathbf{v} + \nabla \cdot (\mathbf{v} \mathbf{v}) - (\nabla \cdot \mathbf{v}) \mathbf{v}] + \frac{1}{\mu_0} [\nabla \mathbf{B} \cdot \mathbf{B} - \nabla \cdot (\mathbf{B} \mathbf{B}) + (\nabla \cdot \mathbf{B}) \mathbf{B}] \\ &\rho [-\nabla \mathbf{v} \cdot \mathbf{v} + \nabla \cdot (\mathbf{v} \mathbf{v})] + \frac{1}{\mu_0} [\nabla \mathbf{B} \cdot \mathbf{B} - \nabla \cdot (\mathbf{B} \mathbf{B})] \end{aligned}$$

since $(\nabla \cdot \mathbf{B}) = 0$ and $(\nabla \cdot \mathbf{v}) = 0$. Substituting $v^2 = \frac{M_A B^2}{\rho \mu_0}$ into $\rho \nabla \mathbf{v} \cdot \mathbf{v}$, we get

$$\begin{aligned}\rho \nabla \mathbf{v} \cdot \mathbf{v} &= \rho \nabla \left(\frac{M_A \mathbf{B}}{\sqrt{\mu_0 \rho}} \right) \cdot \left(\frac{M_A \mathbf{B}}{\sqrt{\mu_0 \rho}} \right) \\ &= \frac{1}{\mu_0} [(M_A \nabla \mathbf{B} + \mathbf{B} \nabla M_A) \cdot \mathbf{B} M_A] \\ &= \frac{1}{\mu_0} (M_A^2 \nabla \mathbf{B} \cdot \mathbf{B} + B^2 M_A \nabla M_A).\end{aligned}$$

The left hand side of (4.11) then becomes

$$\begin{aligned}\nabla \cdot (\rho \mathbf{v} \mathbf{v}) - \frac{1}{\mu_0} (M_A^2 \nabla \mathbf{B} \cdot \mathbf{B} + \mathbf{B} M_A^2 \cdot \nabla M_A) + \frac{1}{\mu_0} (\nabla \mathbf{B} \cdot \mathbf{B}) - \frac{1}{\mu_0} \nabla \cdot (\mathbf{B} \mathbf{B}) \\ &= \nabla \cdot \left(\rho \mathbf{v} \mathbf{v} - \frac{\mathbf{B} \mathbf{B}}{\mu_0} \right) + \frac{1}{\mu_0} (1 - M_A^2) (\nabla \mathbf{B} \cdot \mathbf{B}) - \frac{1}{\mu_0} B^2 M_A \nabla M_A \\ &= \nabla \cdot \left(\frac{M_A^2}{\mu_0} \mathbf{B} \mathbf{B} - \frac{1}{\mu_0} \mathbf{B} \mathbf{B} \right) + \frac{1}{\mu_0} (1 - M_A^2) (\nabla \mathbf{B} \cdot \mathbf{B}) - \frac{1}{\mu_0} B^2 M_A \nabla M_A \\ &= \frac{1}{\mu_0} \nabla \cdot [(M_A^2 - 1) \mathbf{B} \mathbf{B}] + \frac{1}{\mu_0} (1 - M_A^2) (\nabla \mathbf{B} \cdot \mathbf{B}) - \frac{1}{\mu_0} B^2 M_A^2 \nabla M_A\end{aligned}$$

Taking the right hand side of (4.11),

$$\begin{aligned}-\nabla p - \rho \frac{\nabla v^2}{2} &= -\nabla p - \frac{\rho}{2} \nabla \left(\frac{M_A^2 B^2}{\rho \mu_0} \right) \\ &= -\nabla p - \frac{1}{2 \mu_0} (M_A^2 \nabla B^2 + B^2 \nabla M_A^2).\end{aligned}$$

Combining all of the terms of (4.11),

$$\begin{aligned}
& \frac{1}{\mu_0} \nabla \cdot [(M_A^2 - 1) \mathbf{B} \mathbf{B}] + \frac{1}{\mu_0} (1 - M_A^2) (\nabla \mathbf{B} \cdot \mathbf{B}) - \frac{1}{\mu_0} B^2 M_A \nabla M_A \\
& = -\nabla p - \frac{1}{2\mu_0} (M_A^2 \nabla B^2 + B^2 \nabla M_A^2) \\
& \frac{1}{\mu_0} \nabla \cdot [(M_A^2 - 1) \mathbf{B} \mathbf{B}] + \frac{1}{2\mu_0} (1 - M_A^2) \nabla B^2 - \frac{1}{2\mu_0} B^2 \nabla M_A^2 \\
& = -\nabla p - \frac{1}{2\mu_0} (M_A^2 \nabla B^2 + B^2 \nabla M_A^2) \\
& \frac{1}{\mu_0} \nabla \cdot [(M_A^2 - 1) \mathbf{B} \mathbf{B}] = -\nabla p - \frac{1}{2\mu_0} \nabla B^2 \\
& \nabla \cdot [(1 - \alpha) \mathbf{B} \mathbf{B}] = \mu_0 \nabla \left(p + \frac{B^2}{2\mu_0} \right)
\end{aligned} \tag{4.12}$$

where $\alpha = M_A^2$. Taking another substitution, $\mathbf{C} = (1 - \alpha) \mathbf{B}$,

$$\begin{aligned}
& \mu_0 \nabla \left(p + \frac{B^2}{2\mu_0} \right) = \nabla \cdot (\mathbf{C} \mathbf{B}) \\
& = (\nabla \cdot \mathbf{C}) \mathbf{B} + (\mathbf{B} \cdot \nabla) \mathbf{C} \\
& = (\nabla \mathbf{C}) \cdot \mathbf{B} - \mathbf{B} \times (\nabla \times \mathbf{C}) \\
& = \nabla [(1 - \alpha) \mathbf{B}] \cdot \mathbf{B} - \mathbf{B} \times (\nabla \times \mathbf{C}) \\
& = -\nabla \alpha (\mathbf{B} \cdot \mathbf{B}) + (1 - \alpha) \nabla \mathbf{B} \cdot \mathbf{B} - \mathbf{B} \times (\nabla \times \mathbf{C}) \\
& = (1 - \alpha) \nabla \left(\frac{B^2}{2} \right) - B^2 \nabla \alpha - \mathbf{B} \times (\nabla \times \mathbf{C}) \\
& = \nabla \left[(1 - \alpha) \frac{B^2}{2} \right] - \frac{B^2}{2} \nabla \alpha - \mathbf{B} \times (\nabla \times \mathbf{C}).
\end{aligned}$$

Therefore (4.12) becomes

$$\begin{aligned}\mu_0 \left[\nabla \left(p + \frac{B^2}{2\mu_0} - (1-\alpha) \frac{B^2}{2\mu_0} \right) + \frac{B^2}{2\mu_0} \nabla \alpha \right] &= -\mathbf{B} \times (\nabla \times \mathbf{C}) \\ \mu_0 \left[\nabla \left(p + \alpha \frac{B^2}{2\mu_0} \right) + \frac{B^2}{2\mu_0} \nabla \alpha \right] &= -\mathbf{B} \times (\nabla \times \mathbf{C}).\end{aligned}\tag{4.13}$$

By breaking down \mathbf{B} and \mathbf{C} into their components, and noting that $\mathbf{B}_t \times (\nabla \times \mathbf{C})_t = 0$ because there is no z -component of the gradient ($\frac{\partial}{\partial z} = 0$), the triple cross product $\mathbf{B} \times (\nabla \times \mathbf{C})$ becomes

$$\begin{aligned}\mathbf{B} \times (\nabla \times \mathbf{C}) &= (\mathbf{B}_t + B_z \hat{z}) \times [(\nabla \times \mathbf{C})_t + (\nabla \times \mathbf{C})_z] \\ &= \mathbf{B}_t \times (\nabla \times \mathbf{C})_z + B_z \hat{z} \times (\nabla \times \mathbf{C})_t \\ &= (\nabla A_z \times \hat{z}) \times (\nabla \times \mathbf{C})_z + B_z \hat{z} \times (\nabla C_z \times \hat{z}) \\ &= -(\nabla \times \mathbf{C})_z \nabla A_z + B_z \nabla C_z.\end{aligned}\tag{4.14}$$

$$\begin{aligned}(\nabla \times \mathbf{C})_z &= \nabla \times (1-\alpha) \mathbf{B}_t \\ &= \nabla \times [(1-\alpha) (\nabla \times \mathbf{A})_t] \\ &= -\nabla \alpha \times (\nabla A_z \times \hat{z}) + (1-\alpha) \nabla \times (\nabla A_z \times \hat{z}) \\ &= -(\nabla \alpha \cdot \hat{z}) \nabla A_z + (\nabla \alpha \cdot \nabla A_z) \hat{z} + (1-\alpha) [(\nabla \cdot \hat{z}) \nabla A_z - (\nabla \cdot \nabla A_z) \hat{z}] \\ &= -(1-\alpha) \nabla^2 A_z \hat{z}\end{aligned}$$

$$\begin{aligned}
\nabla \cdot \mathbf{C} &= \nabla \cdot [(1-\alpha) (\nabla \times \mathbf{A})] = 0 \\
(1-\alpha) \nabla \cdot (\nabla \times \mathbf{A}) + (\nabla \times \mathbf{A}) \cdot \nabla (1-\alpha) &= 0 \\
-(\nabla A_z \times \hat{z}) \cdot \nabla \alpha &= \nabla A_z \cdot \nabla \alpha = 0
\end{aligned}$$

$$\begin{aligned}
B_z \nabla C_z &= B_z \nabla [(1-\alpha) B_z] \\
&= B_z [B_z \nabla (1-\alpha) + (1-\alpha) \nabla B_z] \\
&= -B_z^2 \nabla \alpha + (1-\alpha) \nabla \left(\frac{B_z^2}{2} \right) \\
&= -B_z^2 \nabla \alpha + \nabla \left[(1-\alpha) \frac{B_z^2}{2} \right] + \frac{B_z^2}{2} \nabla \alpha \\
&= \frac{1}{2} \nabla [(1-\alpha) B_z^2] - \frac{B_z^2}{2} \nabla \alpha
\end{aligned} \tag{4.15}$$

$$-\mathbf{B} \times (\nabla \times \mathbf{C}) = -[(1-\alpha) \nabla^2 A_z] \nabla A_z - \frac{1}{2} \nabla [(1-\alpha) B_z^2] + \frac{B_z^2}{2} \nabla \alpha \tag{4.16}$$

Once again replacing $A = A_z$,

$$\begin{aligned}
\mu_0 \left[\nabla \left(p + \alpha \frac{B^2}{2\mu_0} \right) + \frac{B^2}{2\mu_0} \nabla \alpha \right] &= -[(1-\alpha) \nabla^2 A] \nabla A - \frac{1}{2} \nabla [(1-\alpha) B_z^2] + \frac{B_z^2}{2} \nabla \alpha \\
\mu_0 \nabla \left[p + \alpha \frac{B^2}{2\mu_0} + (1-\alpha) \frac{B_z^2}{2\mu_0} \right] &= -[(1-\alpha) \nabla^2 A] \nabla A + \left(\frac{B_z^2 - B^2}{2} \right) \nabla \alpha \\
\mu_0 \nabla A \frac{d}{dA} \left[p + \alpha \frac{B^2}{2\mu_0} + (1-\alpha) \frac{B_z^2}{2\mu_0} \right] &= -[(1-\alpha) \nabla^2 A] \nabla A + \left(\frac{B_z^2 - B^2}{2} \right) \nabla A \frac{d\alpha}{dA} \\
\mu_0 \frac{d}{dA} \left[p + \alpha \frac{B^2}{2\mu_0} + (1-\alpha) \frac{B_z^2}{2\mu_0} \right] &= -(1-\alpha) \nabla^2 A + \left(\frac{B_z^2 - B^2}{2} \right) \frac{d\alpha}{dA}
\end{aligned}$$

$$\begin{aligned}
\mu_0 \frac{d}{dA} \left[p + \alpha \frac{B^2}{2\mu_0} + (1-\alpha) \frac{B_z^2}{2\mu_0} \right] &= -(1-\alpha) \nabla^2 A + \left(\frac{B_z^2 - B^2}{2} \right) \frac{d\alpha}{dA} \\
\mu_0 (1-\alpha) \frac{d}{dA} \left[p + \alpha \frac{B^2}{2\mu_0} + (1-\alpha) \frac{B_z^2}{2\mu_0} \right] &= -(1-\alpha)^2 \nabla^2 A + (1-\alpha) \left(\frac{B_z^2 - B^2}{2} \right) \frac{d\alpha}{dA} \\
\mu_0 \frac{d}{dA} \left[(1-\alpha) \left(p + \alpha \frac{B^2}{2\mu_0} + (1-\alpha) \frac{B_z^2}{2\mu_0} \right) \right] + \mu_0 \frac{d\alpha}{dA} \left[p + \alpha \frac{B^2}{2\mu_0} + (1-\alpha) \frac{B_z^2}{2\mu_0} \right] &= -(1-\alpha)^2 \nabla^2 A + (1-\alpha) \left(\frac{B_z^2 - B^2}{2} \right) \frac{d\alpha}{dA} \\
\mu_0 \frac{d}{dA} \left[(1-\alpha) p + \alpha (1-\alpha) \frac{B^2}{2\mu_0} + (1-\alpha)^2 \frac{B_z^2}{2\mu_0} \right] + \mu_0 \frac{d\alpha}{dA} \left[p + \frac{B^2}{2\mu_0} \right] &= -(1-\alpha)^2 \nabla^2 A
\end{aligned}$$

Substituting $P'_t = (1-\alpha)p + \alpha(1-\alpha)\frac{B^2}{2\mu_0} + (1-\alpha)^2\frac{B_z^2}{2\mu_0}$, $A' = (1-\alpha)A$,

and taking the special case $\alpha \equiv const.$,

$$\begin{aligned}
\mu_0 \frac{dP'_t}{dA} &= \mu_0 \frac{dP'_t}{dA'} \frac{dA'}{dA} = -(1-\alpha)^2 \nabla^2 A \\
\mu_0 (1-\alpha) \frac{dP'_t}{dA'} &= -(1-\alpha) \nabla^2 A' \\
\mu_0 \frac{dP'_t}{dA'} &= -\nabla^2 A'
\end{aligned}$$

4.2 Automated GS-based detection of SFRs

In both the original and the GS-type equations, the transverse pressure P_t , and its equivalent P'_t , are single variable functions of the magnetic flux function A (A' for the GS-type with $\alpha \equiv const$). With this feature, one can recover the 2D cross-section of a flux rope structure from the 1D spacecraft data by solving the initial value problem based on the GS equation, i.e., by carrying out the GS reconstruction procedures (Hau and Sonnerup, 1999; Hu and Sonnerup,

2002; Hu, 2017). The GS-based techniques in this study consist of the GS-type reconstruction and the extended GS-based automated detection. Considering the complicated environment from the solar wind to the magnetosheath, we adopt the GS-type reconstruction in this study for selected events only.

A cross section of a cylindrical flux rope structure is fully characterized by the 2D scalar flux function $A(x, y)$, and the field-line invariants (B_z, J_z, p, P_t) vary among the nested cylindrical flux surfaces while remaining constant on each distinct surface with a distinct A value (Hu et al., 2018). As a spacecraft passes through the cross section of a magnetic flux rope with closed transverse field lines, it crosses the same set of magnetic field lines twice, the second time being in reverse order as the first half of the crossing. Therefore, the measured magnetic flux function A associated with the field lines traversed by the spacecraft is double-folded, meaning there is a turning point at which an extremum in A is reached. These features, especially the double-folding pattern, are the basis for the GS reconstruction-based identification algorithm (Hu et al., 2018). Figure 4.1 shows diagram of a reconstruction of a magnetic cloud event and the associated flux rope structure. The cross section from the reconstruction algorithm can be seen as well as its relation to the magnetic field lines of the flux rope structure. A more detailed description of the implementation (Hu et al., 2018), including a flowchart of the flux rope detection algorithm, can be found in Appendix 6.2, and online¹.

The GS-based algorithm starts by moving a window continually through an entire data segment with variable window sizes in turn, ranging from the

¹fluxrope.info/flowchart.html

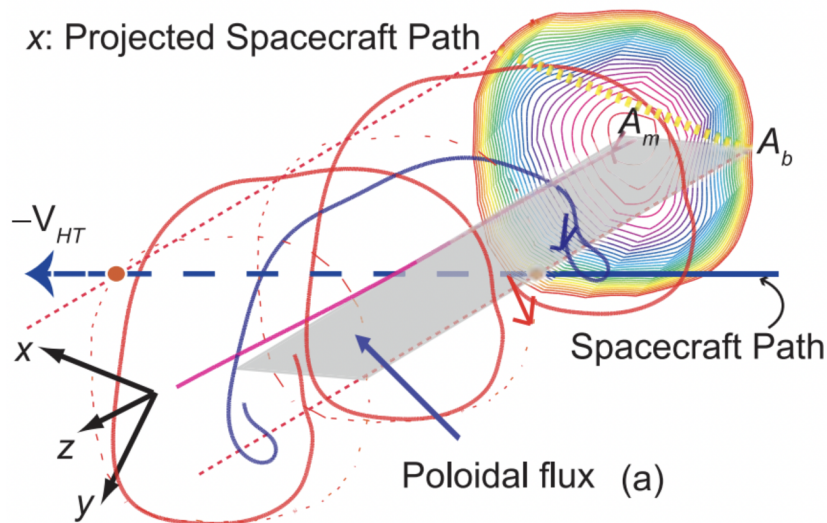


Figure 4.1: View of a flux rope structure reconstruction for a magnetic cloud event (Hu et al., 2015) as a spacecraft passes through it. The 2D cross section and selected associated magnetic field lines (red and blue twisted lines) are shown along the flux rope axis (z -axis). The variables A_m and A_b mark the magnetic flux function A at the center and boundary, respectively, of the reconstruction result. The poloidal flux and axial flux can also be obtained through the reconstruction algorithm.

minimum duration of approximately 10 data points with cadence Δt , i.e. $10\Delta t$, to the maximum duration of 343 data points to cover a wide range of SFR duration, while taking into account limited computing resources. The maximum duration corresponds to approximately 17 minutes for the THEMIS data, and 25 minutes for the MMS data. The in situ magnetic field and plasma data from a specified window of time are first transformed into the co-moving frame, notably the de Hoffmann-Teller frame (de Hoffmann and Teller, 1950). Through a trial-and-error process, the optimal orientation of the z -axis is determined. A trial z -axis is represented by the azimuthal and polar angles, ϕ and θ , in the GSE coordinate system. The azimuthal angle ϕ is the longitude of the SFR z -axis, which measures the angle between the GSE X -direction and the projection of the z -axis onto the XY -plane. The polar angle θ is the angle between the SFR z -axis and the Z -direction. To do so, we select trial values for ϕ and θ , and calculate the transverse pressure P'_t along the spacecraft path, as shown in Equation (4.10). The plot of P'_t versus A' may have a turning point where P'_t along the spacecraft path splits into two parts, with an extreme A' value near this turning point, typically for an SFR structure. This is where the magnetic field B_y component changes sign because of the field line geometry of a helical structure. Figure 4.2 represents such a P'_t versus A' plot, with two distinct portions joining near a turning point with a minimum A' value. We evaluate the quality of the folding (or overlapping) of the two parts of P'_t versus A' by two metrics, R_{diff} (the point-wise difference residue between the two parts) and R_{fit} (a residue of the fitting function $P'_t(A')$ as illustrated by the solid black curve). These metrics are used to check how well the two parts

fold onto each other, provided that such a turning point exists. The threshold conditions, $R_{diff} \lesssim 0.2$ and $R_{fit} \lesssim 0.2$ for these metrics, are selected empirically to guarantee good double-folding quality (Hu et al., 2018). We are able to find the optimal orientation of the z -axis of the SFR by going through iterations of ϕ and θ until the minimum residue values are found. Once the minimum residues satisfying the threshold conditions are found, the corresponding optimal z -axis orientation and event interval are recorded as an SFR candidate.

After the initial detection of SFR candidates, the list of initial candidates is refined. The records are further classified based on the Walén test slope w , which is the slope of the linear regression between $\mathbf{V}_{\text{sw}} - \mathbf{V}_{\text{HT}}$ and \mathbf{V}_A . Records with $|w| \leq 0.3$ are quasi-static SFRs and thus saved directly. Records with $|w| > 0.3$, except for when the correlation coefficient r between the aforementioned two velocities ($\mathbf{V}_{\text{sw}} - \mathbf{V}_{\text{HT}}$ and \mathbf{V}_A) is $|r| \geq 0.8$ and $\langle M_A \rangle \leq 0.9$, are removed. These conditions ensure that the remaining plasma flow is aligned with the local magnetic field, and also to avoid a singularity in Equation (4.10) at $\alpha = 1$. Events with $\alpha > 1$ are rare, but they are also removed, so that the events remaining are sub-Alfvénic. We also remove events from the initial candidate list if the candidates have a turning point within $5\Delta t$ (turn time) of the turning point of another candidate with a smaller R_{diff} , as these could be the same overlapping structures. Table 4.1 lays out the threshold conditions as utilized in the post-processing of the GS-based detection event list (Chen et al., 2020, 2021; Chen and Hu, 2022). The duration of the search windows does not exceed $343\Delta t$ (~ 25.733 minutes for MMS and ~ 24.553 minutes for THEMIS) due to computational time

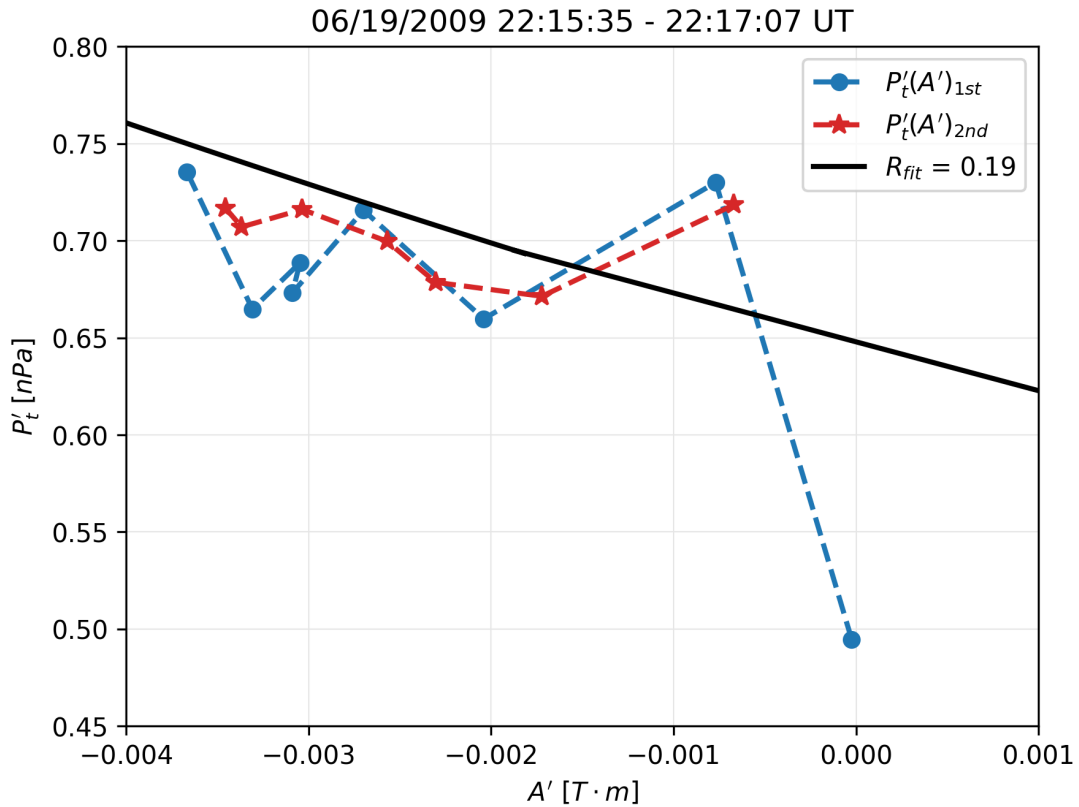


Figure 4.2: The P'_t versus A' plot for an SFR interval from 22:15:35-22:17:05 UT on 19 June 2009 observed by THM-C. The data points are marked by the symbols, and are connected by the blue dashed line and the red dashed line, separated by the turning point at the minimum of A' in this case. The two lines correspond to the first and second parts of the $P'_t(A')$ curve as denoted by the legend. The solid black curve represents a functional fitting to the data points with fitting residue R_{fit} .

constraints. The detection algorithm was performed for some time periods with search window size up to 388 points in duration; however, the search yielded very few (generally less than 3) additional event counts after the post-processing steps. This was due to the step of making sure there is no overlap between SFR candidates, which prioritizes smaller duration candidates. Therefore, with the search algorithm taking a significant amount of time to run for longer search windows and yielding very few results, it was decided to stop the search at the maximum window size of $343\Delta t$. The PyGS software used to reconstruct the 2D cross-section of the events can be found at <https://github.com/PyGSDR/PyGS>.

Table 4.1: Table of threshold conditions for GS reconstruction-based algorithm. R_{diff} and R_{fit} are residues which ensure good double-folding quality in the $P'_t(A')$ vs. A' curve..

Duration	R_{diff}	R_{fit}	Turn time	Walén test slope	$ r $	$\langle M_A \rangle$
$10\Delta t$ - $343\Delta t$	< 0.2	< 0.2	$5\Delta t$	$ w \leq 0.3$		
$10\Delta t$ - $343\Delta t$	< 0.2	< 0.2	$5\Delta t$	$ w > 0.3$	≥ 0.8	≤ 0.9

4.3 2D Reconstructions of cross-sections

Figures 4.4 and 4.5 are examples of the reconstruction of 2D cross-sections of selected flux rope events, both in the magnetosheath. These were reconstructed using the PyGS package. The black lines indicate the transverse magnetic field lines, and the color background indicates the axial field lines B_z with the strength denoted by the color bar. The flux rope structure is confirmed by the closed

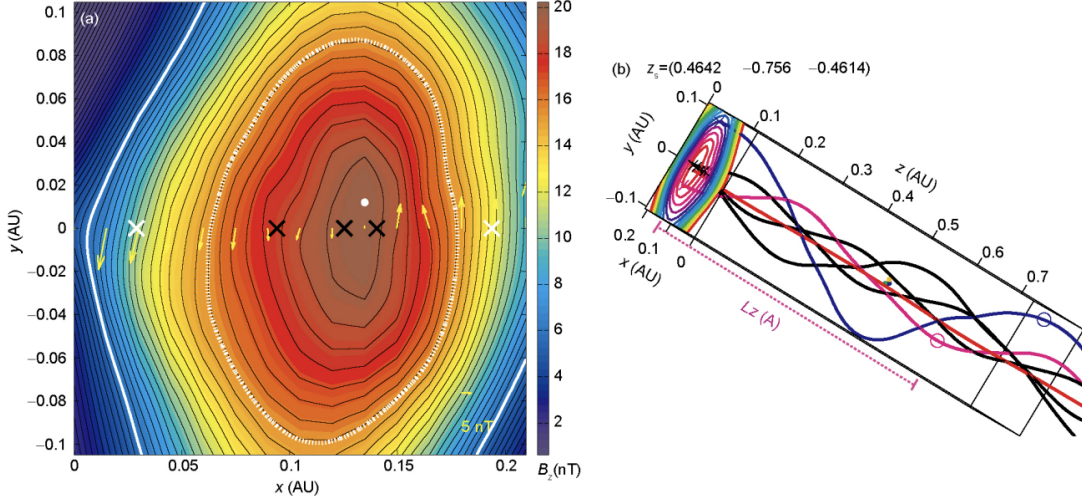


Figure 4.3: Reconstruction of a magnetic cloud (Hu et al., 2015): a) 2D cross section of $A(x, y)$ for a reconstructed magnetic cloud event. The black lines indicate the transverse magnetic field lines, and the color bar indicates the axial field lines B_z . The yellow arrows denote the transverse field lines (B_t) along the path of the spacecraft ($y = 0$). The white contour indicates the area of the reconstruction done from spacecraft data ($A = A_b$), while the area outside the white contour is reconstructed from extrapolation. b) 3D view of a flux rope structure for the magnetic cloud event, showing the 2D cross section (A') and selected associated twisted magnetic field lines along the flux rope axis (denoted at the top). The black field lines rooted at the foot points where the electron onsets were observed. The pink and blue circles denote the locations where the associated field lines complete a full turn around the z -axis.

field lines region and unipolar B_z . The white dot indicates the maximum B_z . The white arrows denote the transverse field lines (B_t) along the path of the spacecraft ($y = 0$), and the green arrows along this path denote the remaining flow velocity. The white contour indicates the area of the reconstruction done from spacecraft data, while the area outside the white contour is reconstructed from extrapolation. The associated time series are displayed below the event reconstructions. The event in Figure 4.4 has a Walén slope of -0.09, and the event in Figure 4.5 has a Walén test slope of 0.002. This indicates that the structures

are static, where the remaining flow vectors (green) along the spacecraft path in the cross-section have little alignment with the transverse magnetic field line vectors (white arrows). The closed, transverse field lines, and the B_t vectors along the spacecraft path show that the reconstruction in Figure 4.4 is a right-handed event, while the structure in Figure 4.5 is a left-handed flux rope. The maximum B_z of the structure in Figure 4.4 is 11.85 nT, and that of the structure in Figure 4.5 is 18.21 nT.

Figure 4.6 shows the reconstruction of a quasi-static event in the magnetosheath. It has a much larger scale size ($\sim 5R_E$) than those in the magnetosheath ($\lesssim 1R_E$). The Walén test slope of this event is 0.399, which meets the $|w| > 0.3$ threshold. It can be seen that the structure has a considerable remaining flow, as indicated by the size of the green arrows.

4.4 Analysis results

Table 4.2 summarizes the events identified in the solar wind and magnetosheath across the identified time periods: 19 in the solar wind and 19 in the magnetosheath simultaneously from two spacecraft, and an additional 58 periods in the solar wind and 111 in the magnetosheath (including those from the refined Toy-Edens et al. (2024a) list). The occurrence rate for events in the solar wind from the GS-based is about 5.1 events/hour and for the magnetosheath the corresponding rate is about 7.3 events/hour. SFRs are observed approximately in 43% and 44% of the total observation periods in the solar wind and magnetosheath, respectively. Properties of the magnetic structures are recorded during

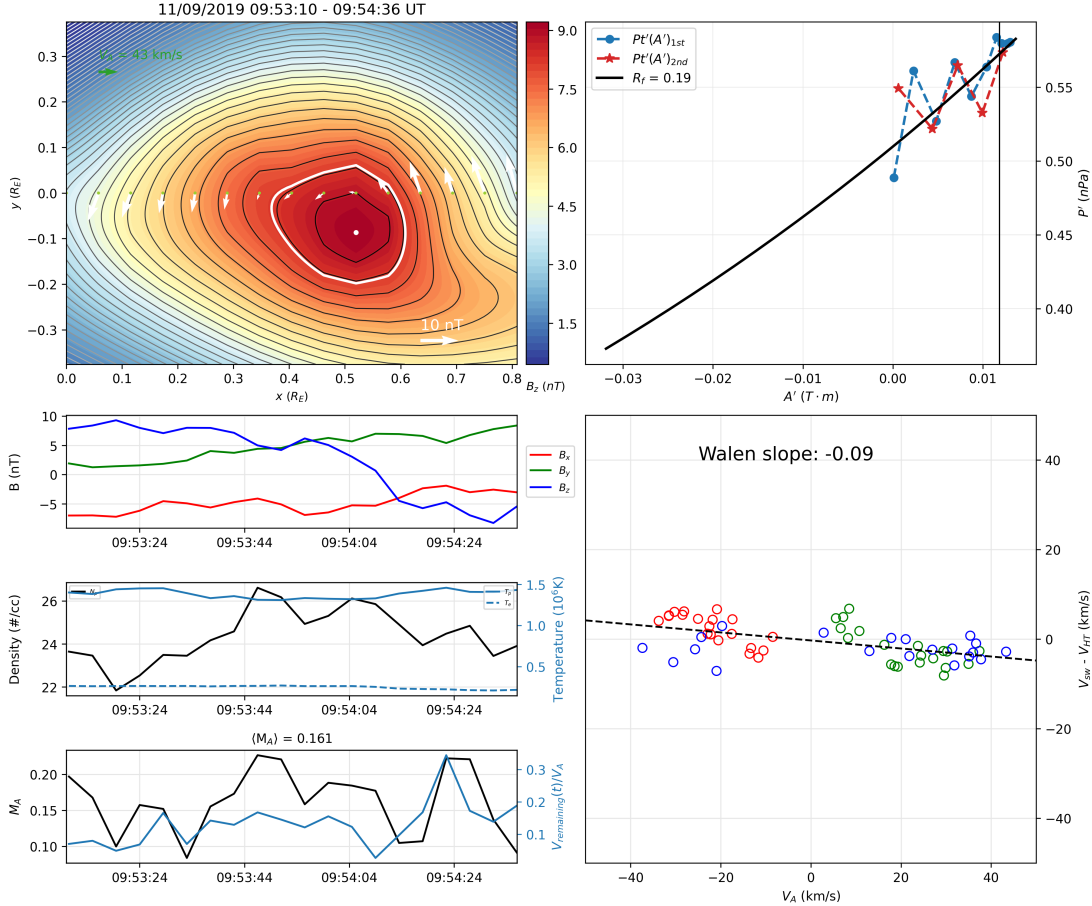


Figure 4.4: GS-based reconstruction of an event 9:53:10–9:54:36 UT on 9 November 2019 in the magnetosheath. Top left: 2D cross-section, with $\hat{x}_{GSE} = [0.890, 0.268, 0.369]$, $\hat{y}_{GSE} = [0.142, 0.605, -0.784]$, $\hat{z}_{GSE} = [-0.433, 0.750, 0.500]$. Bottom left: Associated time series data for MMS-1 in the magnetosheath during this period. Top right: $P'_t(A')$ vs. A' curve for this event. Bottom right: Walén relation for this event.

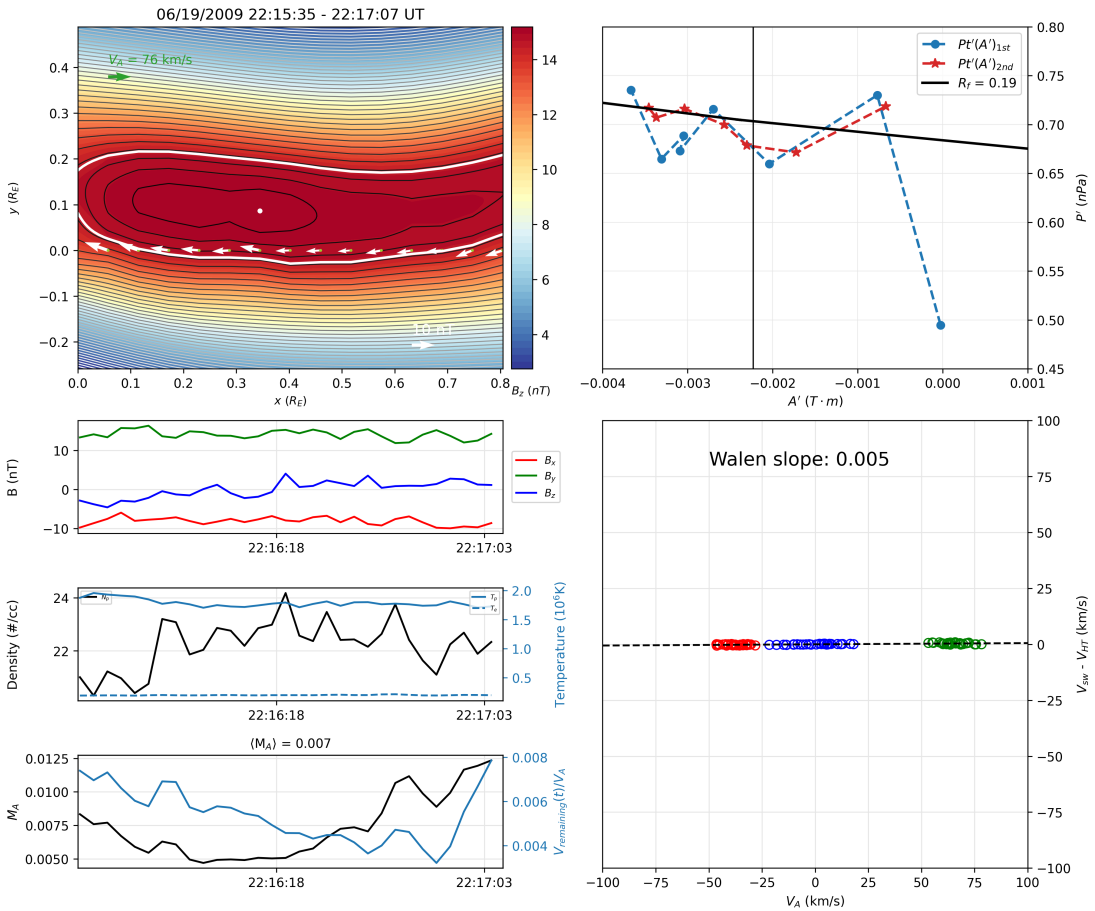


Figure 4.5: GS-based reconstruction of an event from 22:15:35-22:17:07 UT on 19 June 2009 in the magnetosheath. Top left: 2D cross-section, with $\hat{x}_{GSE} = [0.761, -0.103, 0.640]$, $\hat{y}_{GSE} = [0.628, 0.365, -0.688]$, $\hat{z}_{GSE} = [-0.163, 0.925, 0.342]$. Bottom left: Associated time series data for THM-C in the magnetosheath during this period. Top right: $P'_t(A')$ vs. A' curve for this event. Bottom right: Walén relation for this event.

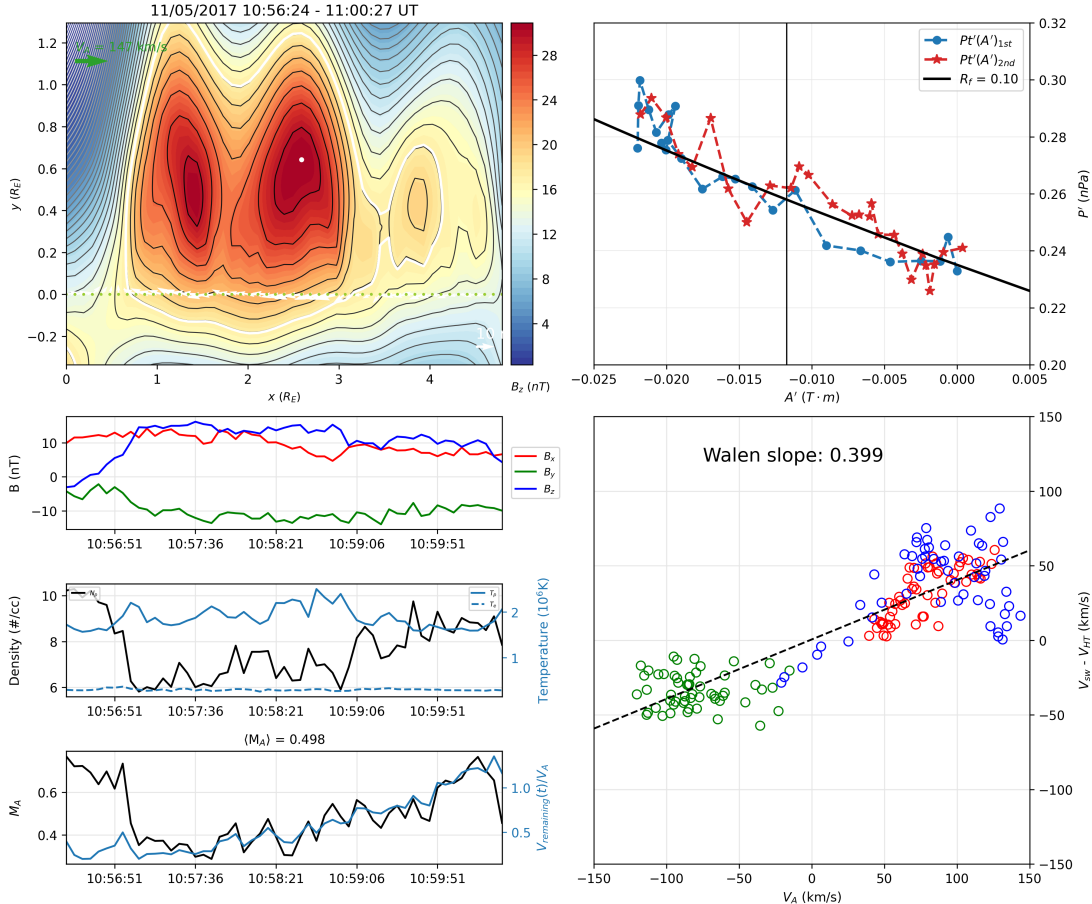


Figure 4.6: GS-based reconstruction of an event on 10:56:24-11:00:27 UT on 5 November 2017 in the magnetosheath. Top left: 2D cross-section, with $\hat{x}_{GSE} = [0.409, -0.029, -0.912]$, $\hat{y}_{GSE} = [0.561, 0.796, 0.226]$, and $\hat{z}_{GSE} = [0.720, -0.604, 0.342]$. Bottom left: Associated time series data for MMS-1 in the magnetosheath during this period. Top right: $P'_t(A')$ vs. A' curve for this event. Bottom right: linear regression of the remaining flow V_{rem} versus the Alfvén velocity V_A , with Walén slope for this event being 0.399.

Table 4.2: Summary table for identified events in the solar wind and magnetosheath via the GS-based reconstruction identification algorithm.

	Observation period [hrs]	Events	Event rate [#/hour]
<i>Solar wind</i>	676 hours	3476	5.1
<i>Magnetosheath</i>	1051 hours	7689	7.3

the identification process. The average duration of the events identified with the GS-based method is 5.03 minutes for the solar wind and 3.57 minutes for the magnetosheath. The average magnetic field for the identified events is 4.8 nT in the solar wind and 21.6 nT in the magnetosheath.

Table 4.3 summarizes the statistical values for the events identified with the GS-based analysis. In the solar wind, there are a large number of events with an average magnetic field of less than 10 nT, whereas in the magnetosheath there are relatively much fewer events with $\langle B \rangle < 10$ nT. The median magnetic field magnitude in the solar wind is 4.3 nT, and 17.9 nT in the magnetosheath. The mean $\langle B \rangle$ in the magnetosheath is ~ 20 nT for all of the events identified. In the solar wind, this number is much smaller around 4.9 nT. As shown in Table 4.3, the duration of the events has similar ranges for the two regions. However, for the scale sizes of the GS events in the magnetosheath, they range from 251.7 km to 6×10^5 km, with a median and mean of 1.6×10^4 km, $\sim 2.5 R_E$ and 3.8×10^4 km, $\sim 6.0 R_E$, respectively. In the solar wind, the corresponding values are from

Table 4.3: Statistical values for the physical quantities of the structures identified with the GS-based analysis. Top: magnetosheath; bottom: solar wind.

	Minimum	Maximum	Mean	Median	Std. Dev.
Duration [min]	0.4	25.7	3.6	1.5	4.8
Velocity [km/s]	12.0	547.8	211.4	203.5	81.1
Temperature [10^6 K]	0.6	29.2	3.2	2.3	2.5
$\langle B \rangle$ [nT]	2.0	95.2	21.6	17.9	12.7
Scale size [km]	251.7	6.0×10^5	3.8×10^4	1.6×10^5	5.6×10^4
<hr/>					
Duration [min]	0.4	25.7	5.0	1.6	6.6
Velocity [km/s]	255.8	666.0	365.7	340.2	87.2
Temperature [10^6 K]	0.1	15.2	3.2	3.1	3.5
$\langle B \rangle$ [nT]	0.7	19.9	4.8	4.3	2.5
Scale size [km]	1296.1	8.6×10^5	9.1×10^4	2.9×10^4	1.3×10^5

1296.1 km to 8.6×10^5 km, and a median (mean) of 2.9×10^4 (9.1×10^4) km, ~ 4.6 (14) R_E .

The GS-based method can generate a set of unique physical parameters (Hu, 2017) as summarized in Table 4.4. They include the approximate axial magnetic flux, Φ_z , a product of $\langle B_z \rangle$ and $\pi(\text{scale size}/2)^2$, the poloidal magnetic flux per meter, $|A_m| = \max(|A|)$, and the approximate helicity density per meter $\Phi_z |A_m|$ (Hu et al., 2014). In addition, the statistics for the proportionality pa-

rameter α are also presented. It generally indicates a modest level of Alfvénicity in both the solar wind and in the magnetosheath. The last two rows in the top and bottom blocks of Table 4.4 provide a proxy to the estimated magnetic helicity per unit volume. No clear differences are seen in the distributions and statistics for Φ_z and $|A_m|$ between the two regions.

Figure 4.7 displays the distributions of the approximation to the axial flux and poloidal flux (per unit length) for events identified via the GS-based automated algorithm. Both distributions follow approximate and similar power laws in both regions. The magnetosheath exhibits events corresponding to the maximum magnitude of $|A_m|$ values larger than that in the solar wind, but these counts are few. The mean $|A_m|$ in the solar wind (0.031 Tm) is only slightly lower than that in the magnetosheath (0.035 Tm), and all corresponding statistical values are of the same orders of magnitude. For completeness, Figure 4.8 shows the distribution of the approximation to the helicity density per unit length. The sample size needs to be enlarged to discern any differences between the two distributions. The statistical values for the helicity density per meter for the events in the magnetosheath are generally of the same orders of magnitude as those in the solar wind, except for the maximum and that the median for the magnetosheath is ~ 2.5 times larger than that of the solar wind. On the other hand, the statistical values for the helicity density per unit volume in the magnetosheath are typically larger than those in the solar wind by one order of magnitude. This is likely an indication of compression of the SFR structures downstream of the bow shock.

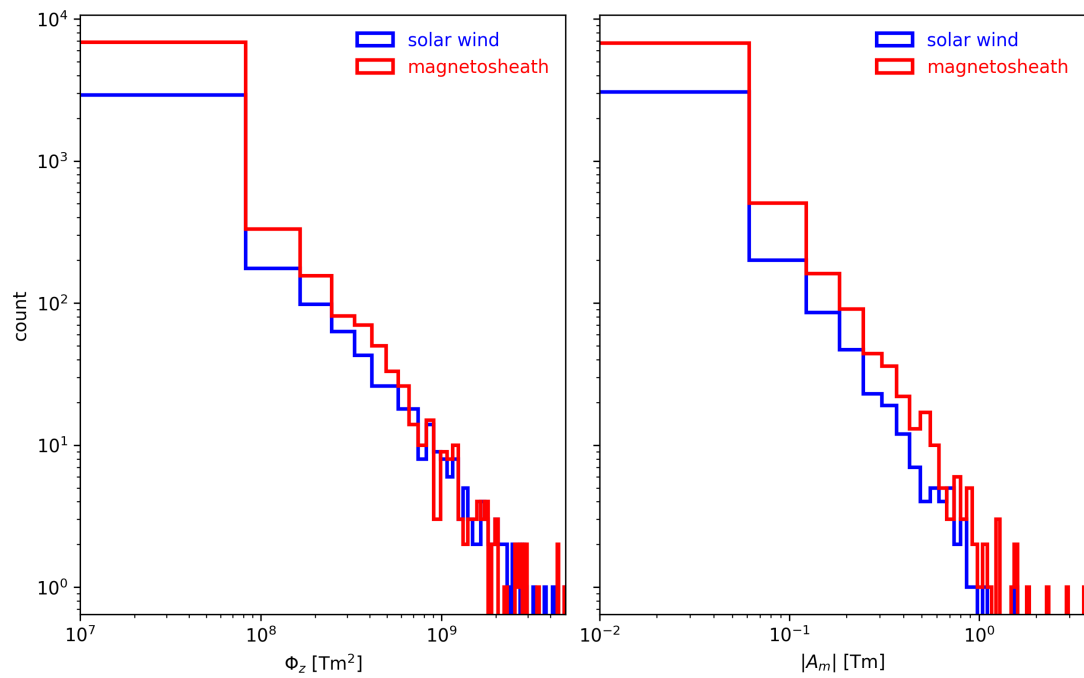


Figure 4.7: Distributions of the axial flux (left panel) and the poloidal flux per unit length (right panel) of events identified via the GS-based analysis. Blue lines are for solar wind events, and red lines for magnetosheath events.

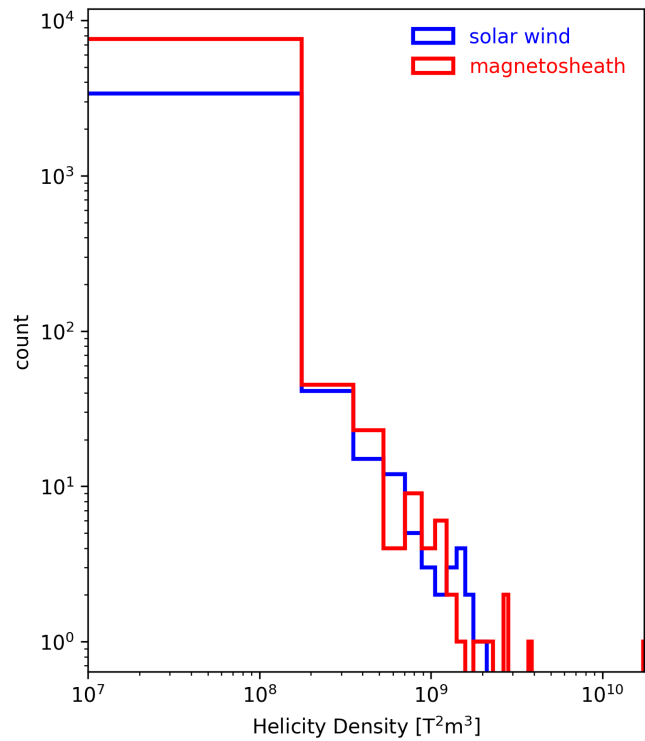


Figure 4.8: Histograms for the approximation to the helicity density per unit length of the events identified via the GS-based analysis for the solar wind (blue) and the magnetosheath (red).

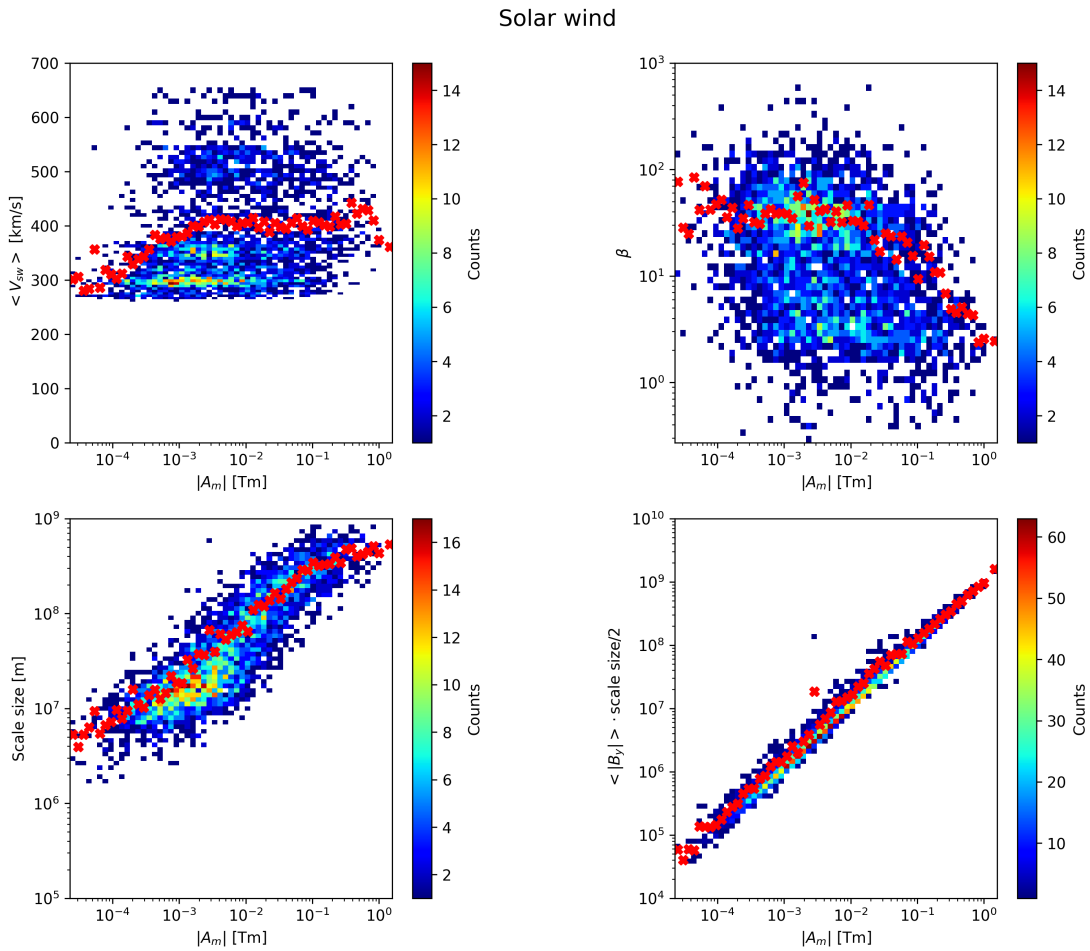


Figure 4.9: Caption

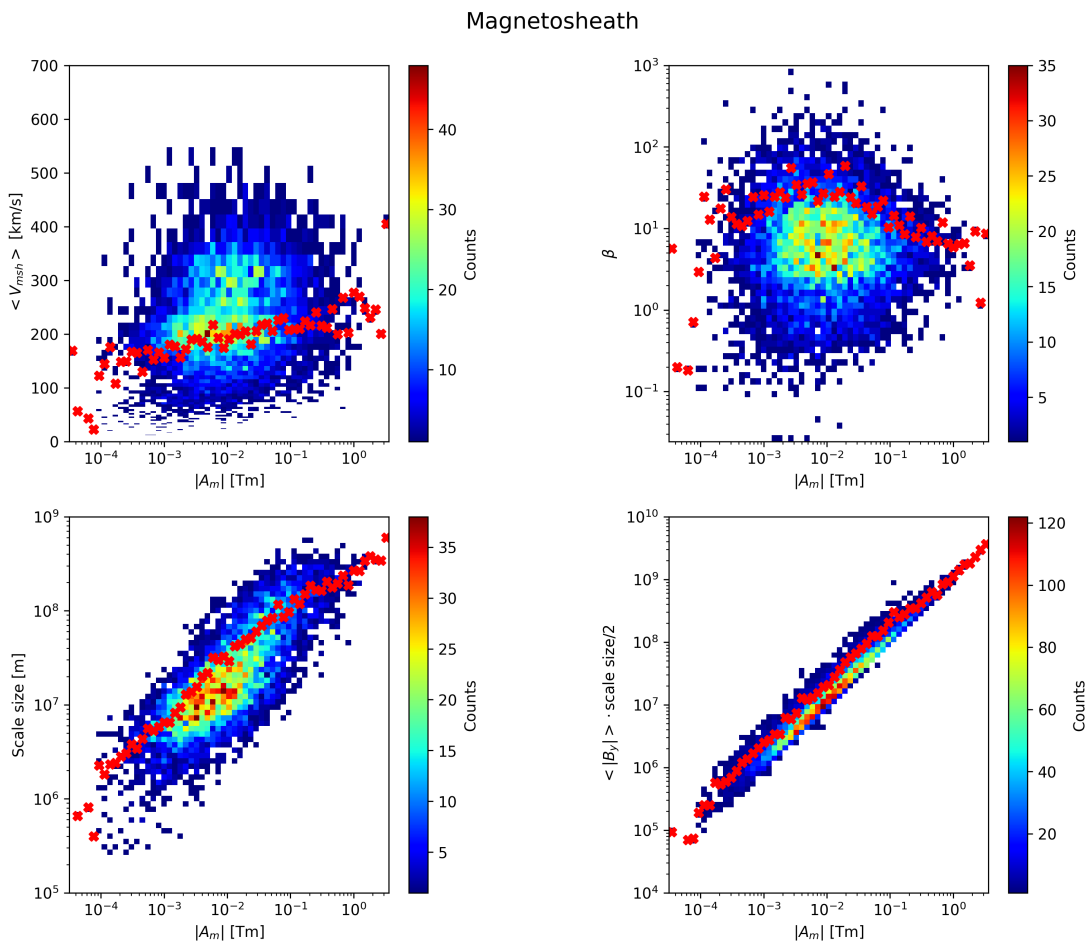


Figure 4.10: Caption

Table 4.4: Statistical values for the physical quantities characterizing the SFR structures identified solely via the GS-based method in the two regions. Top: magnetosheath; bottom: solar wind.

Criteria	Minimum	Maximum	Mean	Median
Φ_z [Tm ²]	403.8	4.8×10^9	4.9×10^7	2.1×10^6
$ A_m $ [Tm]	3.1×10^{-5}	3.6	0.04	9.2×10^{-3}
Helicity Density [T ² m ³]	0.01	1.7×10^{10}	1.4×10^7	1.9×10^4
$\alpha = < M_A >^2$	$ w \leq 0.3$	1.3×10^{-6}	0.99	0.14
	$ w > 0.3$	0.09	0.81	0.37
$\langle A \cdot B_z \rangle$ [T ² m]		4.0×10^{-14}	3.0×10^{-8}	3.1×10^{-10}
				4.7×10^{-11}
$\max(A \cdot B_z)$ [T ² m]		7.4×10^{-14}	1.0×10^{-7}	7.7×10^{-10}
				1.1×10^{-10}
Φ_z [Tm ²]	375.5	4.9×10^9	8.7×10^7	2.1×10^6
$ A_m $ [Tm]	2.3×10^{-5}	1.6	0.03	4.0×10^{-3}
Helicity Density [T ² m ³]	0.01	2.0×10^9	1.9×10^7	6.9×10^3
$\alpha = < M_A >^2$	$ w \leq 0.3$	1.4×10^{-6}	0.81	0.06
	$ w > 0.3$	0.09	0.81	0.34
$\langle A \cdot B_z \rangle$ [T ² m]		1.3×10^{-15}	5.4×10^{-9}	8.8×10^{-11}
				5.3×10^{-12}
$\max(A \cdot B_z)$ [T ² m]		1.9×10^{-15}	1.0×10^{-8}	1.8×10^{-10}
				1.1×10^{-11}

4.5 Walén test and Alfvénicity

As described in Section 4.2, the Walén test slope w is used to further distinguish Alfvénic structures. Figure 4.11 shows the linear regression between $\mathbf{V}_{\text{sw}} - \mathbf{V}_{\text{HT}}$ and \mathbf{V}_A during the event on 9 November 2019 during 9:53:10 - 9:54:36 UT. The Walén slope $w = -0.09$ indicates that this event is a static flux rope-like structure, because the magnitude of the slope is less than 0.3.

The distributions of the reduced cross helicity and residual energy for all identified events with the GS-based reconstruction identification algorithm are shown in Figure 4.12. Like Figure 3.5 (in Section 3.4), Figure 4.12 has a flatter distributions of reduced cross helicity σ_c in the magnetosheath than in the solar wind. Unlike the analogous distributions in Figure 3.5, Figure 4.12 shows that for the GS-based analysis result, there are nearly no events with $\sigma_r > 0$. This is likely due to the intrinsic differences between the two methods. With the GS-based method, we can evaluate the Alfvénicity of the structures with the Walén test slope. Table 4.5 summarizes the classification of the events with the Walén test slope. There is a slightly higher relative number of events with Walén slope $|w| > 0.3$ in the magnetosheath than in the solar wind. The majority (5088) of the 7689 events from the GS-based algorithm in the magnetosheath have Walén test slopes $|w| \leq 0.3$, and 2601 events have Walén slopes $|w| > 0.3$. 1067 events of the 3476 GS-based algorithm events in the solar wind have $|w| > 0.3$, which is a slightly lower proportion compared to that in the magnetosheath.

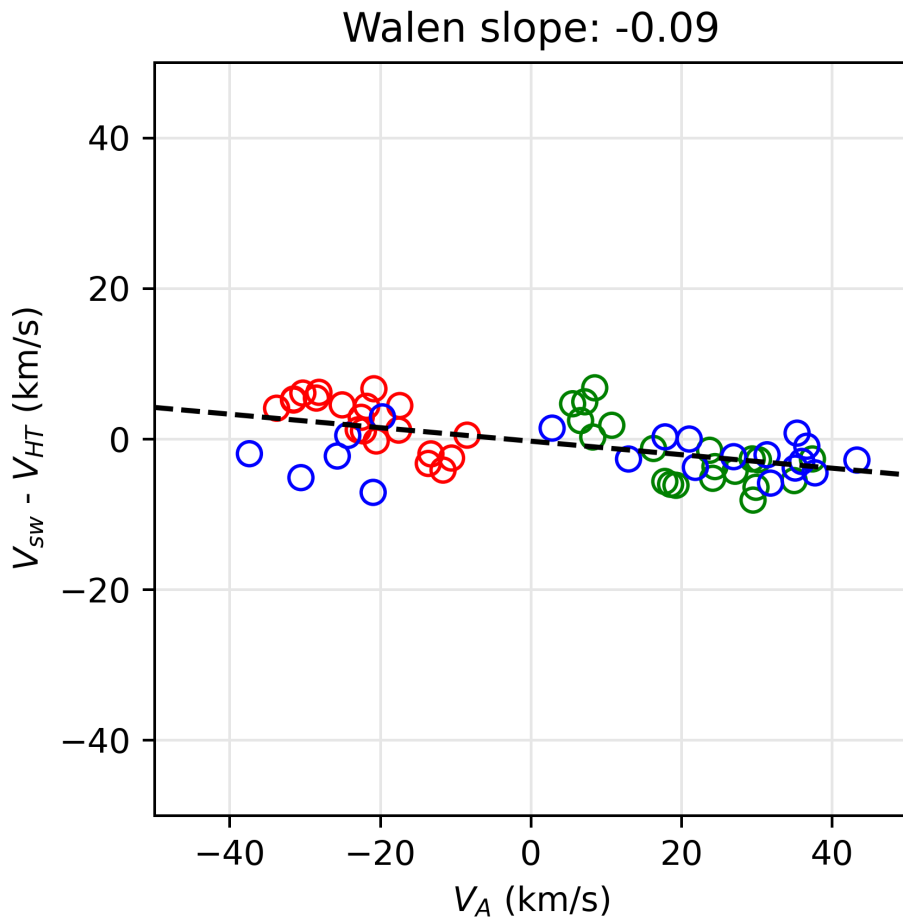


Figure 4.11: Plot of $\mathbf{V}_{\text{sw}} - \mathbf{V}_{\text{HT}}$ and \mathbf{V}_A for 9 November 2019 during 9:53:10 - 9:54:36 UT. The black dashed line is the linear regression between the two quantities, i.e., the Walén slope. The red, green, and blue circles represent the x -, y -, and z - components of the velocities, respectively.

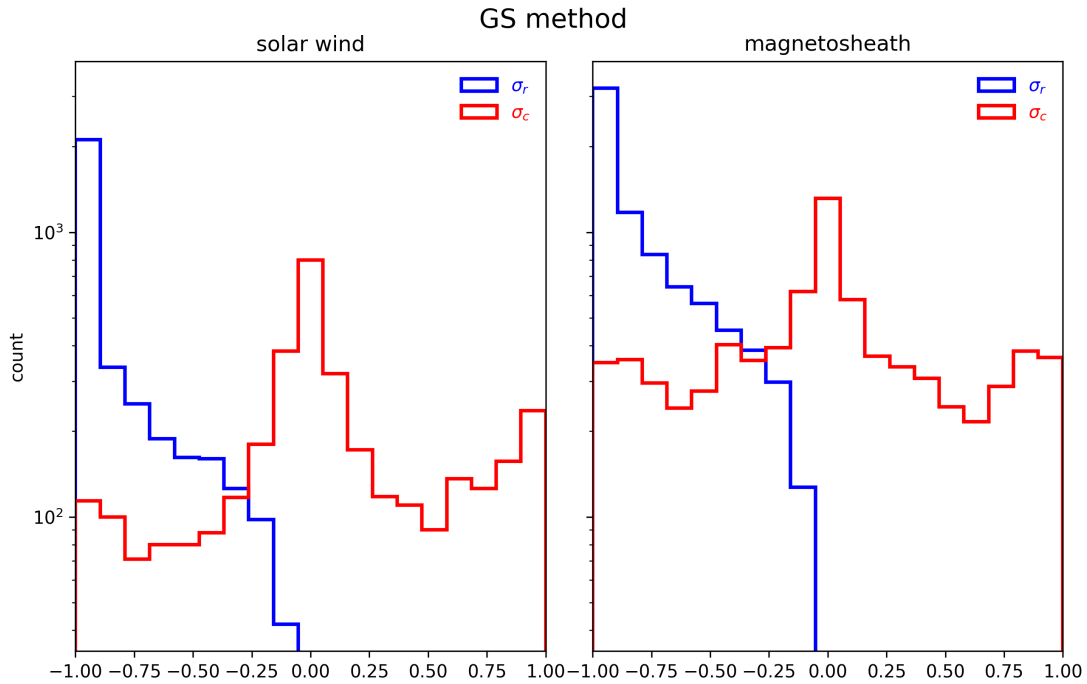


Figure 4.12: Histograms of reduced cross helicity σ_c (red) and reduced residual energy σ_r (blue) for all solar wind (left) and magnetosheath events (right) identified with the GS-based reconstruction identification algorithm.

Table 4.5: Events identified with the GS-based method meeting different Walén test slope criteria.

	Solar wind	Magnetosheath
<i>Total</i>	3476	7689
$ w \leq 0.3$	2409	5088
$ w > 0.3$	1067	2601

It can be seen that events with a high Alfvén Mach number (and thus proportionality constant α) are more prominent in the magnetosheath. The distribution of the proportionality constant α partially represents the data in Tables 4.4 and 4.5. The mean α for events with $|w| \leq 0.3$ was 0.337 and 0.366 for the solar wind and magnetosheath, respectively. For $|w| > 0.3$, the means had a greater difference at 0.059 and 0.139 for the respective regions. The median values for α in the solar wind were 7.575×10^{-3} for $|w| \leq 0.3$ and 0.297 for $|w| > 0.3$. In the magnetosheath, the median values for α were 0.055 and 0.323 for $|w| \leq 0.3$ and $|w| > 0.3$, respectively.

4.6 Flow velocities and orientation of SFRs

Lastly, a representation of the average flow velocities of the identified event intervals, i.e., \mathbf{V}_{HT} vectors, is shown in Figure 4.15. For the identified SFR structures, we find that the corresponding flow velocities in the solar wind are fairly uniform and along the Sun-Earth direction; however, in the magnetosheath the flows appear to be largely deflected toward the duskside flank. Therefore the structures near the flanks (downstream of the quasi-perpendicular portion of the bow shock) ought to have elongated cross sections, resulting in large scale sizes. It is likely that while the structures may be compressed by the bow shock in the dimension along the normal direction of the bow shock, they may experience stretching along the dimension in the direction of the bulk flows, i.e., approximately perpendicular to the normal direction. This explains why some structures

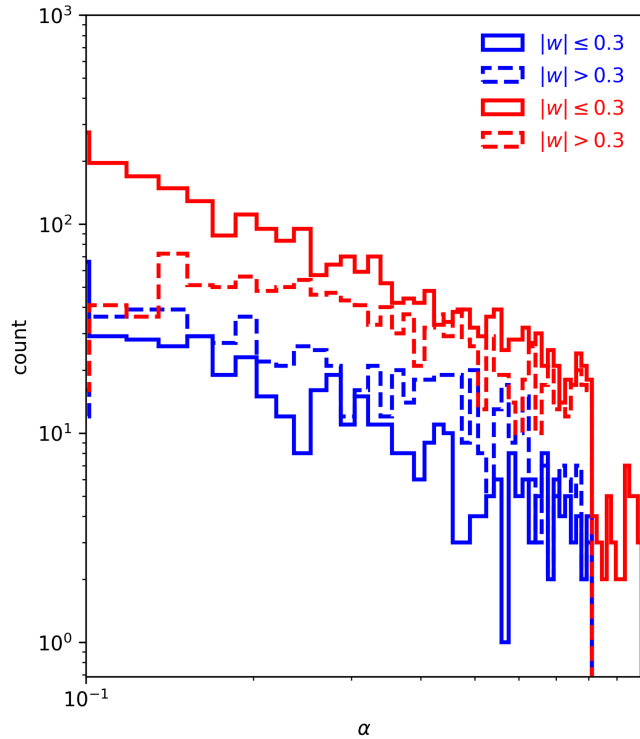


Figure 4.13: Histograms for proportionality constant $\alpha = \langle M_A \rangle^2$ of events identified via GS analysis. For this histogram, blue lines are solar wind events, and red lines are magnetosheath events. Solid lines represent events with a Walén slope $|w| \leq 0.3$ and dashed lines represent events with $|w| > 0.3$.

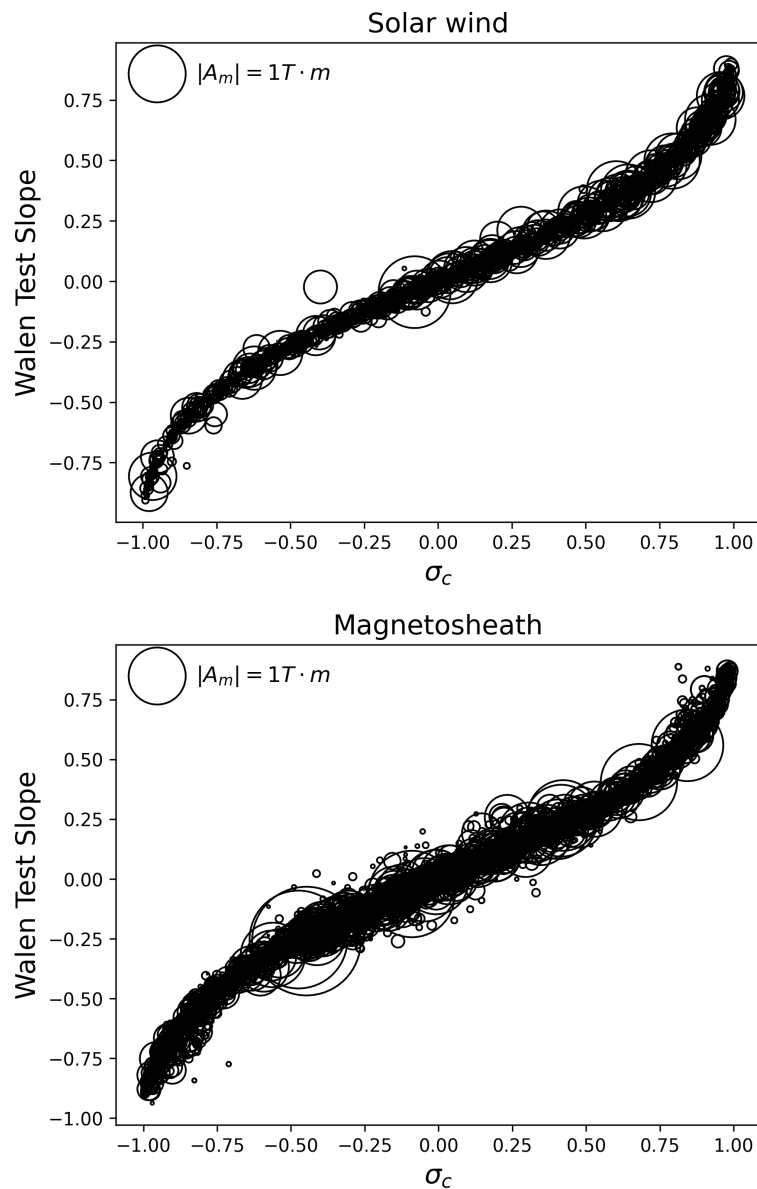


Figure 4.14: Caption

in the magnetosheath have large scale sizes, for instance, larger than the typical width of the magnetosheath itself.

Figure 4.16 shows the histograms of the z -axis orientation angles of the structures identified from the GS-based algorithm. For the solar wind, there is a single peak in the polar angle distribution centered around 60-70 degrees; however, for the magnetosheath there are two prominent peaks: one around 20-40 degrees and another from around 120-140 degrees. There is a significant trough in the distribution for the magnetosheath events around 80-100 degrees. The azimuthal angle has a flatter distribution in the solar wind than in the magnetosheath. The azimuthal angles in the solar wind show a small dip in the distribution around 170 degrees, and correspondingly there are two narrower peaks for the azimuthal angle in the magnetosheath, around 100 degrees and 260-300 degrees, possibly separated by 180 degrees. The shift in the dip between the two distributions is small, going from about 170 to 200 degrees for the two regions. Overall, the distributions of the azimuthal angle maintain similar shapes in the two regions, except for an additional enhanced peak near $\Phi \approx 0$ in the magnetosheath. The significant change in the polar angle in the magnetosheath indicates that the structures likely experience a rotation in the orientation downstream of the bow shock. It is possible that the interaction with the bow shock forces the change in the orientation of the magnetic structures.

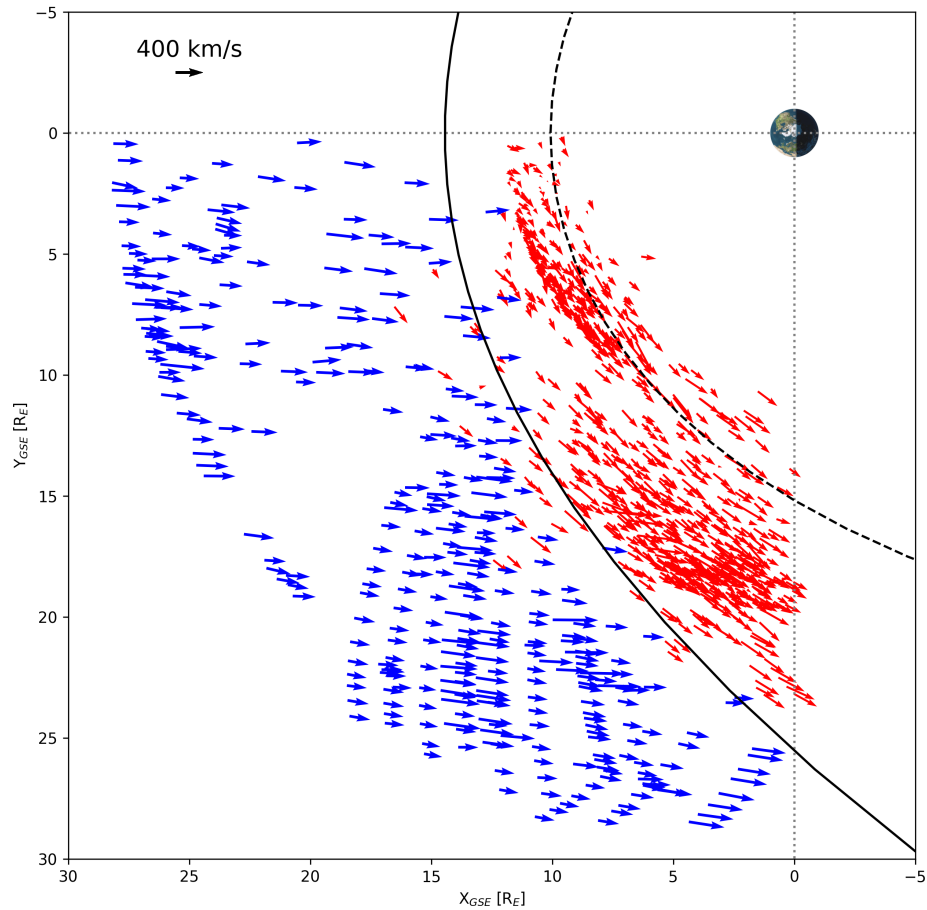


Figure 4.15: Plot showing the \mathbf{V}_{HT} vectors at the locations of one-tenth of the total events identified in the solar wind (blue) and magnetosheath (red) on the GSE- XY plane. The nominal bow shock (solid curve) and magnetopause (dashed curve) locations are drawn based on the models by Shue et al. (1997) and Slavin et al. (1984), respectively. A reference vector of magnitude 400 km/s is shown in the upper left corner.

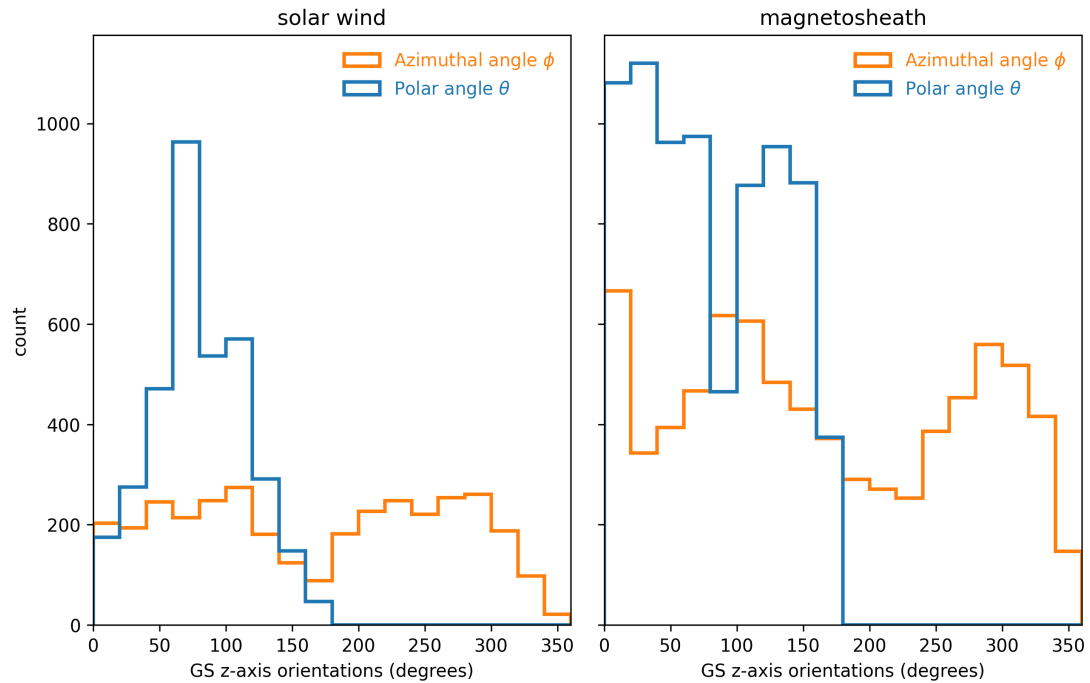


Figure 4.16: Distributions of the azimuthal (orange) and polar angles (blue) of the directional angles that define the z -axis (in the GSE coordinate system) of the SFR structures identified from the GS-based analysis in the solar wind (left panel) and the magnetosheath (right panel).

Chapter 5. Coordinated Analysis

A coordinated analysis between the magnetosheath and solar wind over ~ 250 hours was performed in order to compare simultaneous observations. 19 time intervals were identified during these phases for which there were simultaneous measurements by two THEMIS probes, where one was in the solar wind and one was in the magnetosheath. The dayside science and radiation belt science phases of the THEMIS mission offer optimal configuration for direct comparison of the near-Earth solar wind and magnetosphere, specifically the phases in 2008, 2009, 2018, and 2022. MMS was also used in conjunction with the THEMIS probes for the observation intervals identified in 2022. Table A.3 in 6.2 shows the subsection of observation intervals for this coordinated analysis. Figure 5.1 displays the orbits of THEMIS and MMS during these observation intervals. It should be noted that the data came from simultaneous measurement in two regions during the same interval, *not* a measurement *across* the bow shock.

Figure 2.6 is an example of one observation such period in the magnetosheath during the coordinated analysis. These measurements were taken in the magnetosheath with THM-C, while the measurements in the solar wind were taken with THM-B (Figure 2.7). Following the same procedures as outlined in Section 3.3, 3308 structures were identified in the solar wind, and 3446 structures

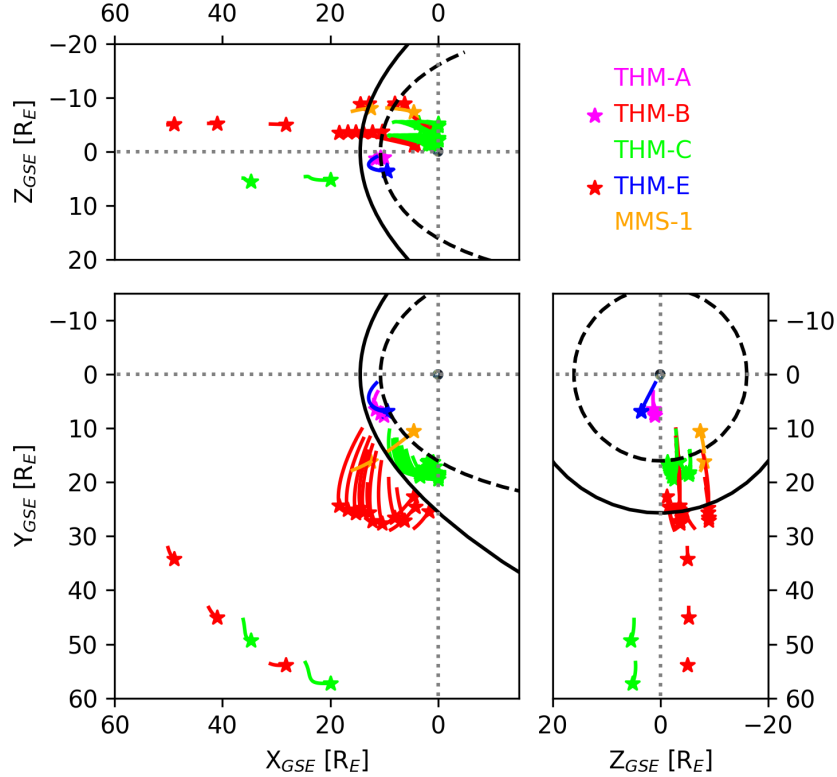


Figure 5.1: Orbits for coordinated analysis time periods are shown in the Geocentric Solar Ecliptic (GSE) coordinates for THEMIS probes A, B, C, and E (THM-A, THM-B, THM-C, THM-E) and MMS-1 probe (see legend), with the stars marking the end of each orbit period. The approximate nominal locations of the magnetopause (dashed black line) modeled using the Shue et al. (1997) model and bow shock (solid black line) modeled using Slavin et al. (1984) are shown, based on the IMF data obtained for one period in 2015 only.

Table 5.1: Summary table for events identified via wavelet analysis and the GS reconstruction algorithm during the simultaneous observation intervals.

Region	Method	# Events	Avg. duration	Avg. B	Avg. scale
			[mins]	[nT]	size [km]
<i>Solar wind</i>	Wavelet	1407	6.43	3.93	1.4×10^5
	GS	1901	3.46	3.90	6.0×10^4
	Total	3308	4.72	3.91	9.3×10^4
<i>Magnetosheath</i>	Wavelet	1179	6.79	13.83	9.1×10^4
	GS	2267	2.66	14.11	2.9×10^4
	Total	3446	4.07	14.02	5.0×10^4

were identified in the magnetosheath during the coordinated intervals. Table 5.1 displays the results for the number of events identified with each method. Table 5.2 shows the characterization of the events for each method according to MHD criteria (wavelet analysis) and Walén slope criteria (GS reconstruction).

It can be seen from Table 5.2 that there were more events characterized as static flux rope structures in the magnetosheath for the coordinated analysis periods. Approximately 79% of the 1179 structures identified in the magnetosheath using wavelet analysis had a reduced cross helicity magnitude less than 0.3. While there were only incrementally more static structures identified in the magnetosheath than in the solar wind; however, the number of static structures represents a higher percentage of the total number of structures in the magnetosheath versus

Table 5.2: Events meeting certain MHD quantity (top) and Walén test slope (bottom) criteria.

		Solar Wind	Magnetosheath
	$ \sigma_m \geq 0.75$	1407	1179
<i>Wavelet</i>	$ \sigma_m \geq 0.75, \sigma_c \leq 0.3$	931	930
	$ \sigma_m \geq 0.75, \sigma_r < 0$	1263	975
	$ \sigma_m \geq 0.75, \sigma_c \leq 0.3, \sigma_r < 0$	853	836
	Total	1901	2267
<i>GS</i>	$ w \leq 0.3$	1777	2197
	$ w > 0.3$	124	70

66% in the solar wind. Approximately 97% of the structures identified in the magnetosheath with the GS reconstruction have a Walén test slope value less than or equal to 0.3 for the coordinated event lists. In the solar wind, the percentage is slightly lower at 93%, despite the number of structures identified with $|w| \leq 0.3$ being over 400 less than the number of structures in the magnetosheath.

The wavelet analysis results for the coordinated periods are complementary to the extended analysis periods, with a larger percentage of structures being identified as static structures in the magnetosheath than in the solar wind. However, in the extended analysis, there was a much smaller difference ($\sim 1\%$) between the two regions. Additionally, there were more structures with $|w| \leq 0.3$ in the solar wind than in the magnetosheath for the extended analysis, which differs

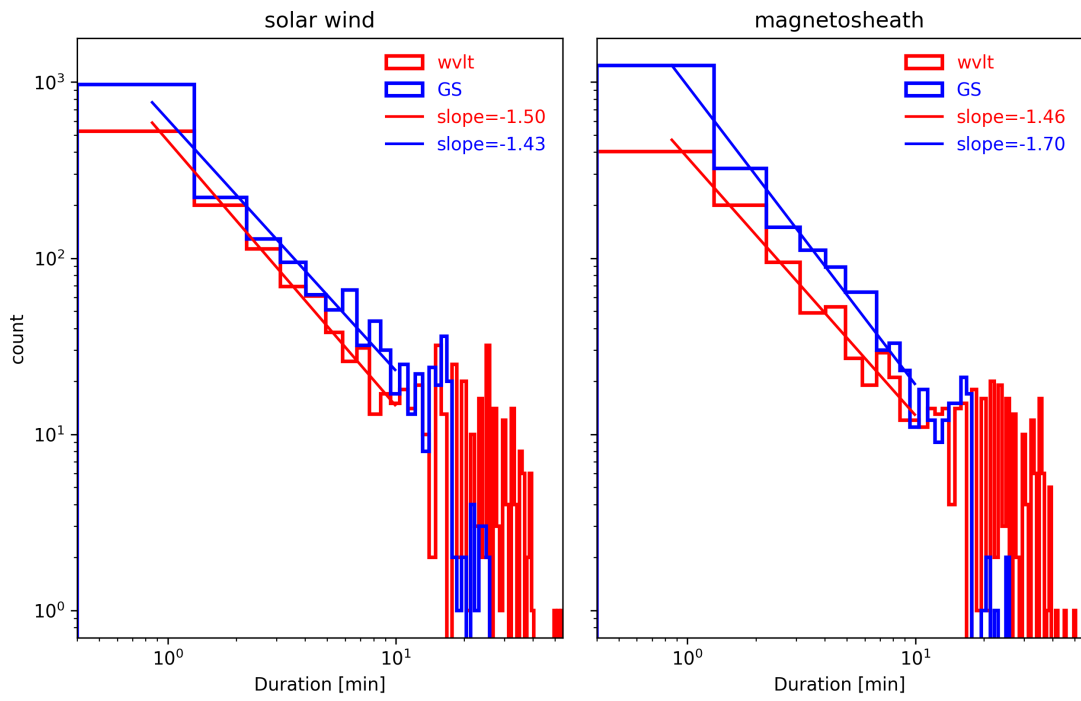


Figure 5.2: Histogram of the duration of events identified (during the coordinated orbit intervals) by using wavelet analysis (red lines) and the GS reconstruction method (blue lines).

from the coordinated analysis. Figures 5.2 through 5.4 show the distributions of selected parameters from events identified during the coordinated intervals.

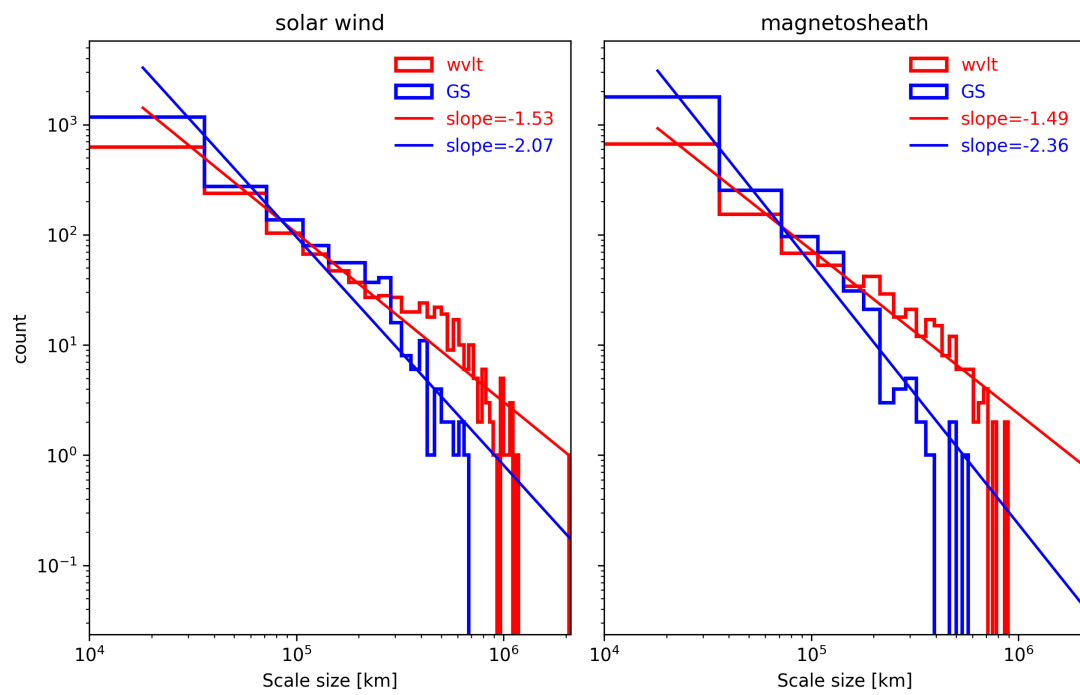


Figure 5.3: Same as Figure 5.2 but for scale size of events identified during the coordinated orbit intervals.

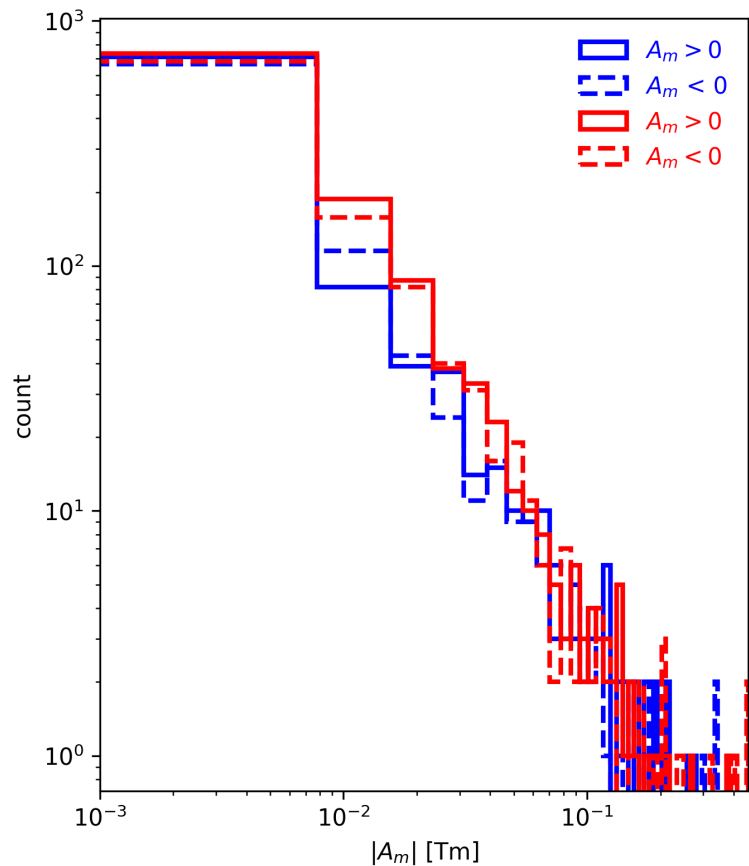


Figure 5.4: Histograms for the local maximum magnetic flux $|A_m|$ of events identified via GS analysis during the coordinated orbit intervals.

Chapter 6. Conclusions and Future Work

6.1 Combined results

Figures 6.1 and 6.2 show the distributions of event duration and structure scale size from events identified with wavelet analysis and the GS-based method. The scale sizes of the solar wind events and the magnetosheath events have a large difference, in part because of the differences in duration. The wavelet events in the solar wind are almost twice as large as the events from the GS-based method. In the magnetosheath, the average scale size of the wavelet events is almost three times as large as that of the GS events. Because of the difference in the minimum and maximum limits of calculating the duration of the events between the wavelet analysis and GS-based methods, the ranges in duration are different. The range of duration for the SFRs identified by the wavelet analysis method is dictated by the time cadence of the spacecraft data (Torrence and Compo, 1998); whereas the duration range of the SFRs identified by the GS-based method can be extended arbitrarily toward the upper limit end (though there are computational limits). The scale size is calculated by taking the average speed of the event interval and multiplying it by the duration of the event for the wavelet analysis. For the SFRs identified by the GS-based method, this calculation is done using the projected de Hoffmann-Teller frame velocity on the cross-sectional plane, which

takes into account the orientation of the cylindrical structure in relation to the spacecraft path thus representing a better cross-sectional size. Whereas such a characterization is not feasible through the wavelet analysis method because like a typical time-series analysis method, it does not characterize structure in dimensions higher than 1D. The scale size calculated in the GS-based method represents a true cross-sectional size for a 2D configuration.

Figure 6.2 shows the corresponding distributions of the scale sizes for the identified events in the magnetosheath and solar wind. They generally follow power laws and the trends indicate that there are more, smaller-size events in the magnetosheath than in the solar wind. This is largely seen through the slope of the scale size distribution of the GS-based method in the magnetosheath, which has a smaller upper limit and a steeper slope than the corresponding distribution in the solar wind. The power-law distributions in Figure 6.2 can indicate anomalous (super- or sub- diffusive) transport. Solar energetic particles (SEPs) can be trapped between the boundaries of two adjacent SFRs (le Roux, 2023), but with power law distributions of SFR scale sizes, the energetic particles can escape to open field lines, i.e., super-diffusive transport. The power law distributions in this work support the theory that when there is energetic particle transport through coherent magnetic structures that create strong, intermittent magnetic fields, the distributions yield a non-Gaussian power law (le Roux and Zank, 2021).

In Figure 6.3, the cumulative distribution functions of the scale sizes further show that there is a larger percentage of smaller structures in the magnetosheath than in the solar wind. For instance in the magnetosheath, the percent-

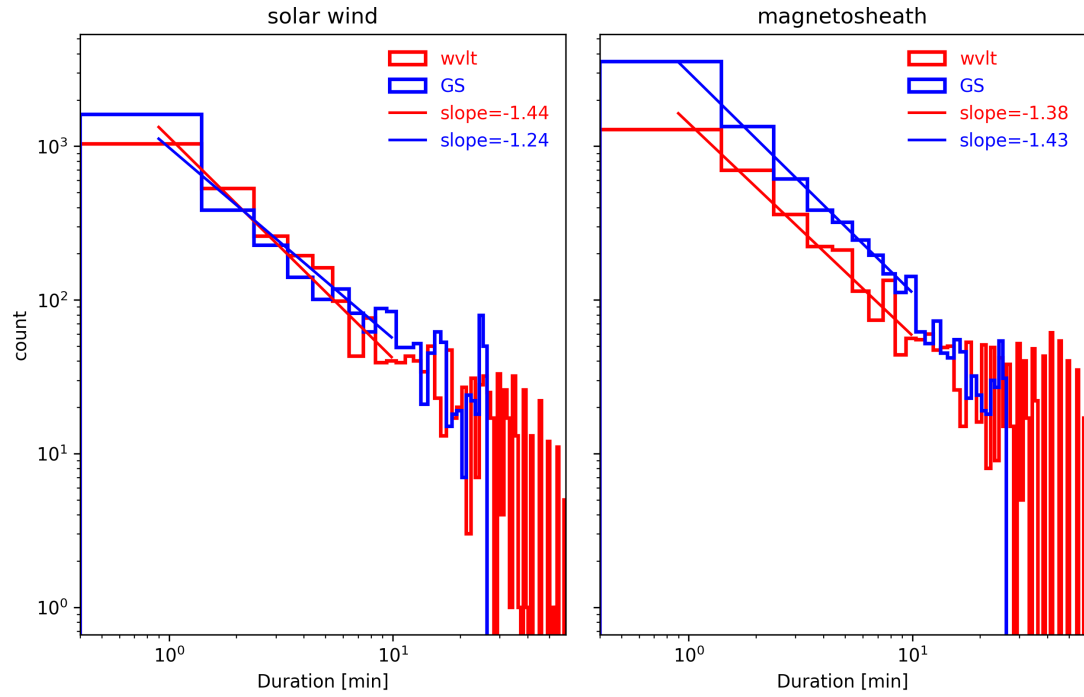


Figure 6.1: Histograms of the duration of events identified by using wavelet analysis (red lines) and the GS-based method (blue lines) in the solar wind (left panel) and magnetosheath (right panel), respectively. The straight lines are the nominal linear fitting to each distribution in a log-log scale with the corresponding slopes denoted in the legend.

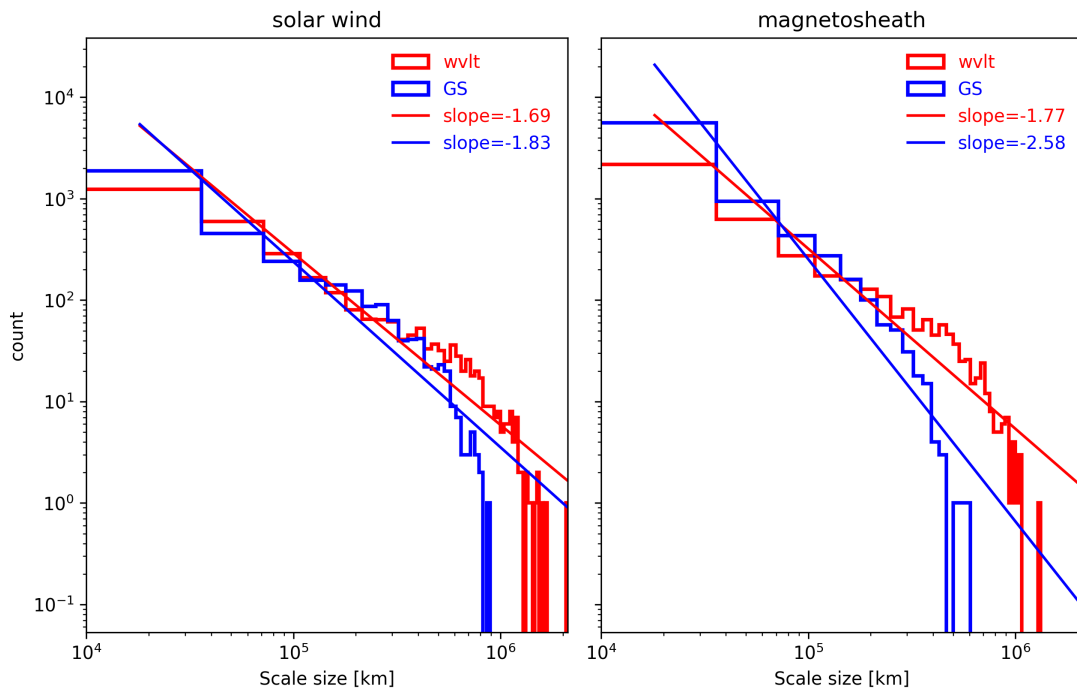


Figure 6.2: Same as Figure 6.1 but for scale size distributions of identified events.

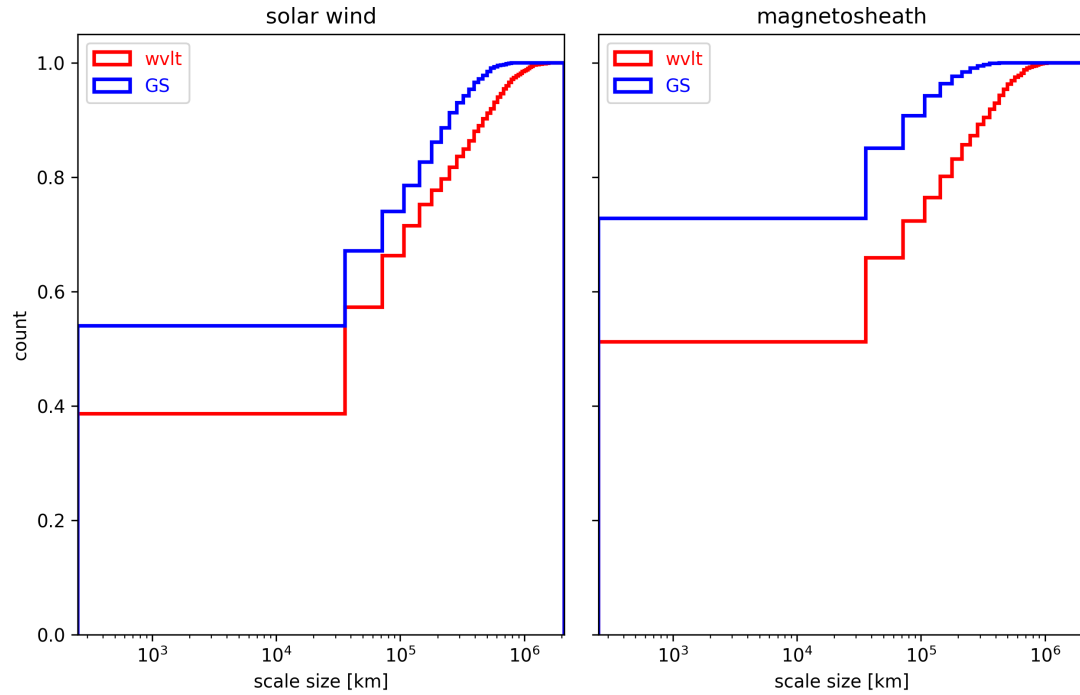


Figure 6.3: Cumulative distribution function of scale sizes for the identified events (see legend) in the solar wind (left panel) and magnetosheath (right panel). The vertical lines mark the corresponding mean values of the scale sizes for the GS-based method for the solar wind (dotted blue lines) and the magnetosheath (dashed blue lines) in both panels.

age of events with scale sizes smaller than the mean value (marked by the dashed line in both panels) is greater than 70% which is significantly larger than the corresponding percentage in the solar wind. The structures generally seem to be compressed across the bow shock: the scale sizes are smaller, and the magnetic field becomes stronger. Furthermore, the maximum scale size of the SFRs in the solar wind is found to be approximately 2 million km, which is on the same order as the turbulence correlation length (Horbury et al., 1996). The power-law distributions are also in agreement with (Nakanotani et al., 2022a,b) which simulated the generation and interaction of smaller scale structures across a shock wave and compared with the turbulence theory (Zank et al., 2021, 2017). Based on our analysis result, since the solar wind is dominated by quasi-2D structures, such as SFRs, the power laws are generally in agreement with the 2D-slab model of turbulence (Zank et al., 2021, 2017).

6.2 Summary

In summary, we have carried out a comprehensive analysis of SFR structures in the regions immediately upstream and downstream of the Earth's bow shock. There were 11949 events identified in the magnetosheath across 1051 hours, with 7689 events being identified from the GS-based algorithm and 4260 from the wavelet analysis. For the solar wind, there were 6669 events identified across 676 hours, with 3476 being attributed to identification via the GS-based algorithm and 3193 via wavelet analysis. We utilized in situ observations of MMS-1, THM-A, THM-B, THM-C, and THM-E spacecraft. We extended the GS-based analysis

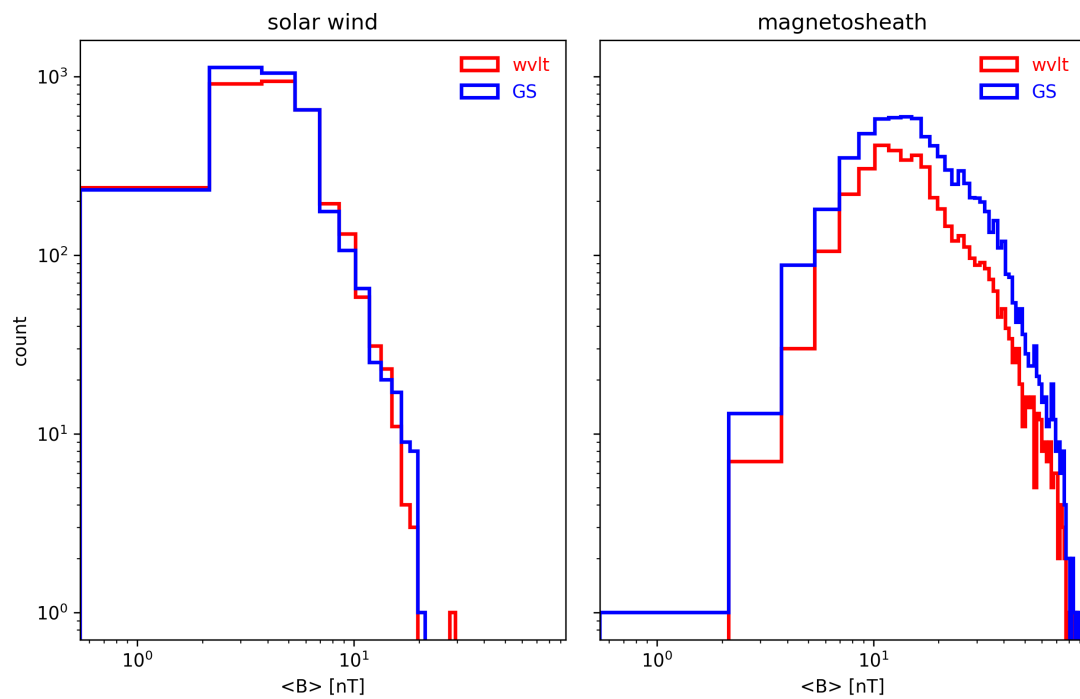


Figure 6.4: Same as Figure 6.1 but for average magnetic field distributions of identified events.

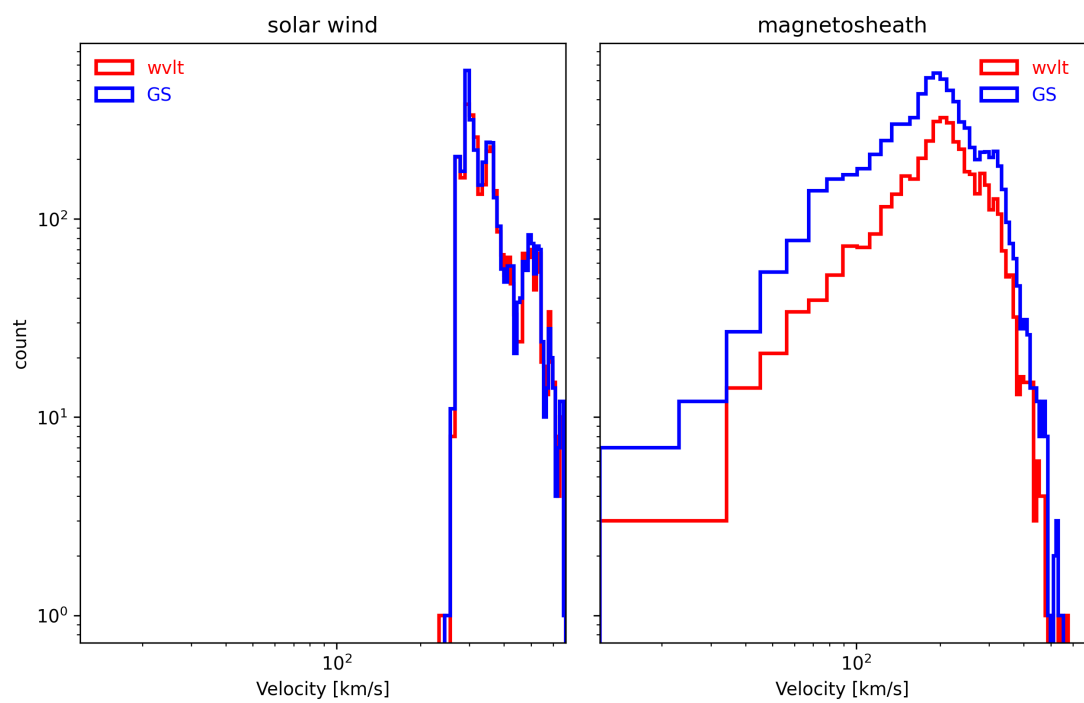


Figure 6.5: Same as Figure 6.1 but for velocity distributions of identified events.

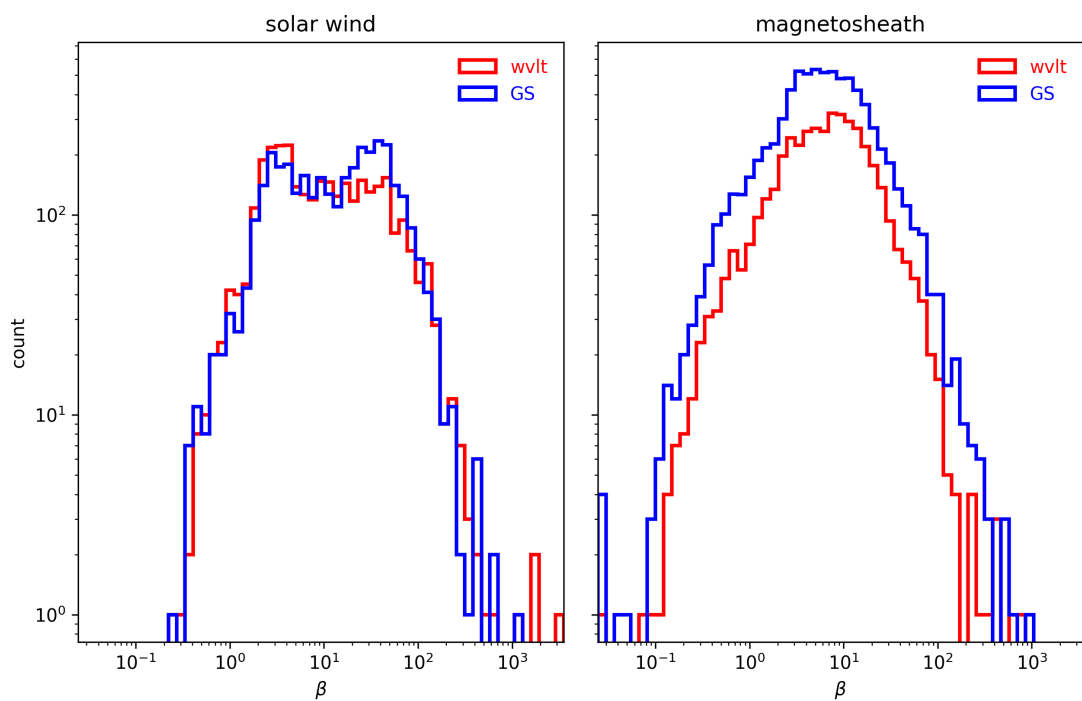


Figure 6.6: Same as Figure 6.1 but for plasma β distributions of identified events.

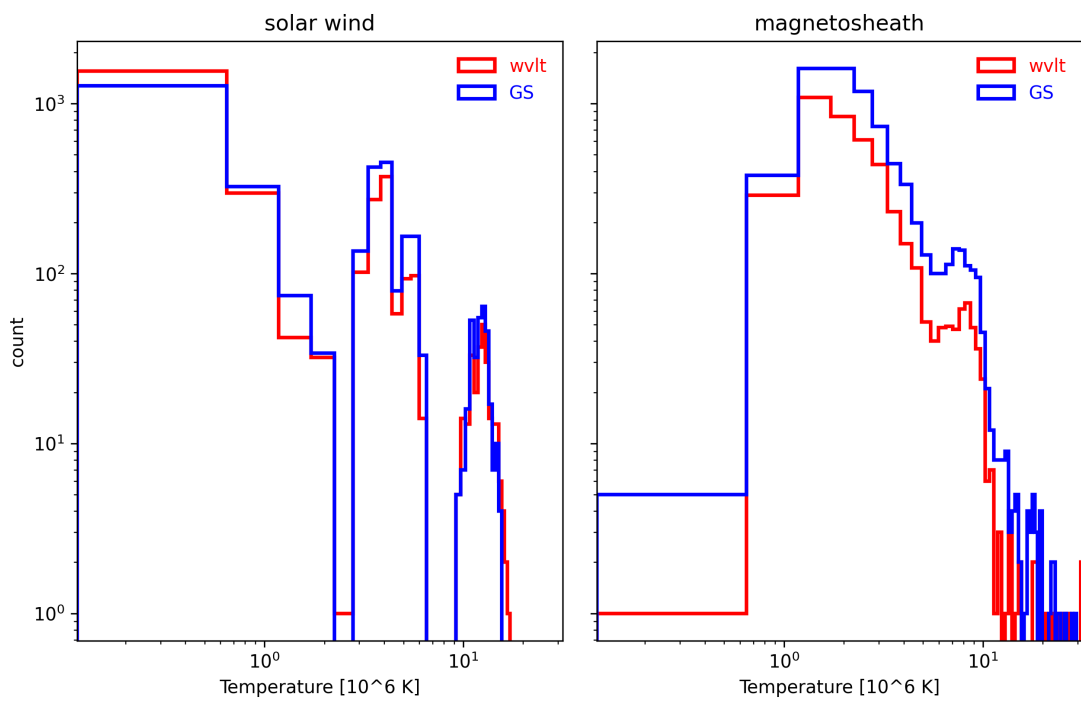


Figure 6.7: Same as Figure 6.1 but for temperature distributions of identified events.

to identify structures with significant remaining plasma flow aligned with the local magnetic field, and also performed wavelet analysis for 77 time periods in the solar wind and 130 time periods in the magnetosheath, corresponding to 676 hours and 1051 hours, respectively. The average magnetic field, velocity, duration, scale size, etc., of these structures were recorded for comparison. In addition to the general parameters, the GS-based method also yielded a unique set of additional parameters that allowed us to evaluate the distributions of the Walén test slope, magnetic helicity density, magnetic flux, and the orientation of the z -axes of the structures.

We showed that the distributions of a wide variety of parameters generally follow power laws. The magnetic structures identified by the wavelet analysis were also characterized based on MHD quantities (σ_m , σ_c , σ_r). The different criteria assisted us to distinguish different types of events in terms of dynamic and quasi-static structures in the two regions. This work intended to examine the differences in the properties primarily obtained from the GS-based characterization of the identified SFR structures in the solar wind and magnetosheath. The additional findings of this study are summarized as follows.

1. The magnitudes of the Walén slope $|w|$ and cross helicity σ_c parameters indicate the effect of the remaining plasma flow of the identified structures. Results from both regions indicate that about one-third of structures possess modest (e.g., $|w| > 0.3$) remaining flow relative to the total number of structures identified.

2. SFR structures are generally compressed downstream of the bow shock in the magnetosheath: the scale sizes are smaller while magnetic field strength increases in the magnetosheath. In addition, the magnetic helicity density per unit volume is about one order of magnitude larger than the corresponding value in the solar wind, implying an overall decrease in volume for the SFRs in the magnetosheath.
3. A significant rotation in the polar angle of the z -axis in the magnetosheath is seen when compared to the angle in the solar wind, while the distributions of the azimuthal angle maintain two broad peaks separated by approximately 180 degrees.